ORIGINAL ARTICLE

lajss.org© Latin American Journal of Solids and Structures

www.lajss.org

Damage Effects of Adjacent Cabin Structures Subjected to Internal Explosions in an Underwater Thin-Walled Steel Box

Yiming Ma[a], Xingbo Xie[a]*, Huayuan Ma[a], Guili Yang[a], Xinghua Li[a], Mingshou Zhong[a]

[a] College of Field Engineering, Army Engineering University of PLA, Nanjing 210007, P. R. China. Email: 2977076757@qq.com, 693757953@qq.com, 503812350@qq.com, 50509100@qq.com, 379523589@qq.com, 109125659@qq.com

* Corresponding author

https://doi.org/10.1590/1679-7825/e9182

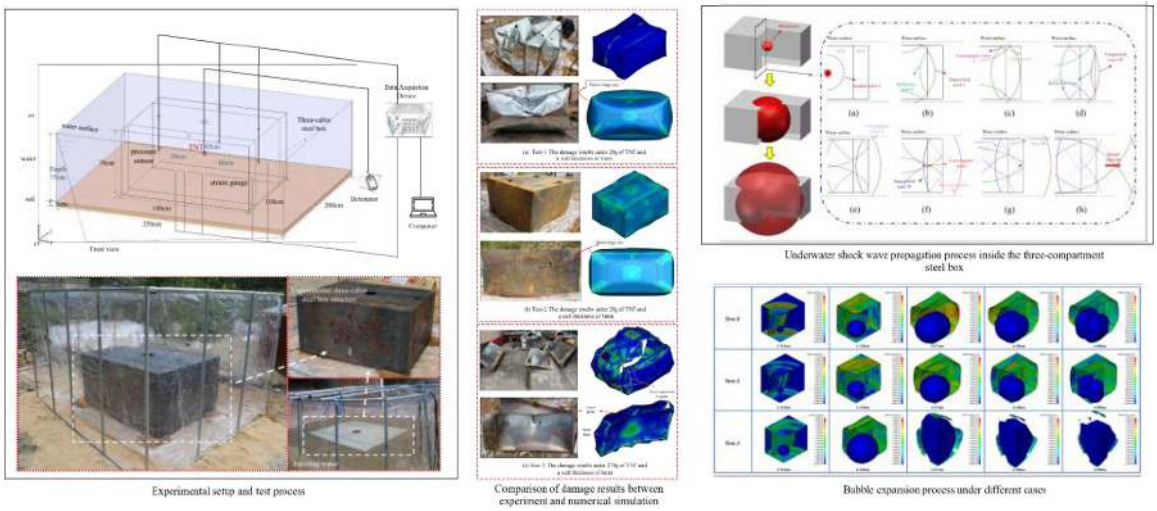
Abstract

This study examines damage effects of internal explosions in an underwater thin-walled steel box on neighboring cabins, integrating experiments and numerical modeling of a three-cabin steel box. It analyzes propagation, dynamic response, and damage effects of explosion loads from the central cabin on adjacent ones. Results show adjacent cabin pressure histories display multiple peaks and extended positive phases, from combined shock wave transmission through the internal bulkhead and reflected waves in the adjacent cabin. Explosion bubble expansion and contraction are largely confined to the central cabin, or escape through ruptured regions. Without perforation in the separating plate, the bubble typically does not penetrate adjacent cabins. Under internal explosion loading, adjacent cabin bulkhead deformation and fracture are primarily induced by transmitted bubble expansion effects. With increasing charge mass, adjacent cabin damage evolves from plastic deformation to edge cracking and shear failure; increased wall thickness reduces damage extent: the 1-mm box disintegrates at 100 g, while the 3-mm box only cracks at 200 g.

Keywords

Underwater internal explosion; Three-cabin steel box; Explosive load characteristics; Damage effects of adjacent cabin structures; Structural dynamic response

Graphical Abstract



Received June 24, 2026. In revised form August 19, 2026. Accepted August 20, 2026. Available online August 21, 2026.
https://doi.org/10.1590/1679-7825/e9182

Latin American Journal of Solids and Structures. ISSN 1679-7825. Copyright © 2026. This is an Open Access article distributed under the terms of the Creative Commons Attribution license, which permits unrestricted use, distribution, and reproduction in any medium, provided the original work is properly cited.

1 INTRODUCTION

Frequent shipwreck incidents associated with contemporary maritime accidents present significant risks to navigation safety and underwater infrastructure (Tørnes and Novik, 2025). In order to restore navigational routes efficiently, internal blast cutting followed by segmented salvage has been demonstrated to offer improved economic and operational effectiveness. For large ships comprising multiple cabins, explosive charges are generally required in each compartment, which leads to increased time consumption and reduced efficiency. Employing a single charge to affect multiple adjacent cabins would substantially enhance the efficiency of blasting and cutting procedures. Investigation of the effects of internal structural configuration and spatial arrangement within a wreck on the transmission characteristics of internal explosion loads into neighboring compartments, the progression of bulkhead fracture, and the performance of blast cutting requires a detailed analysis of the damage mechanisms induced by internal explosions in submerged cabins on adjacent structures. Such investigations provide considerable engineering relevance for improving underwater blast cutting and salvage strategies, while also offering important scientific insights into the propagation behavior of explosion loads in multi-cabin submerged systems.

Structural damage induced by external underwater explosions demonstrates significant complexity, leading to extensive experimental and numerical research efforts by scholars worldwide (Gao, et al., 2024; Peng, et al., 2021; Wang, et al., 2022). Gao et al. (2024) examined the blast resistance and failure behavior of sandwich panels under external explosion loading through integrated experimental and numerical analyses. Peng et al. (2021) employed the Smoothed Particle Hydrodynamics (SPH) and Reproducing Kernel Particle Method (RKPM) to numerically simulate structural damage caused by near-field underwater contact explosions, focusing on the failure mechanisms of representative broadside structures. Wang et al. (2022) analyzed the dynamic response of shipborne liquid tanks subjected to external underwater contact explosions, with emphasis on deformation and tearing failure of both external and internal plates. Cheng et al. (2024) performed comparative analyses of structural responses and damage mechanisms under external explosion loads in different media, specifically air and water, for multi-cabin configurations.

In terms of damage effects resulting from internal explosions within confined cabin structures, considerable attention has also been directed toward the damage effects resulting from internal explosions within structures (Zhang, et al., 2022; He, et al., 2023; Zhang, et al., 2023). In comparison with external explosions, internal explosions exhibit more intricate load characteristics, failure patterns, and spatial distributions, attributed to repeated shock wave reflections within confined spaces and the containment effect of detonation products (Lee, et al., 2017; Kristoffersen, et al., 2019; Yao, et al., 2017; Lin, et al., 2024). Yuan et al. (2021) investigated the role of standoff distance on the inelastic deformation of square steel plates subjected to fully confined internal blast loads in air, combining experimental observations with numerical simulations. Zheng et al. (2016, 2018) studied the response behavior of stiffened plate structures under internal blast loading in air and conducted comparative evaluations of displacement and deformation modes. Qin et al. (2022) carried out eleven internal explosion experiments on reinforced cabin models in an air environment, examining their dynamic response characteristics and failure mechanisms under such loading conditions. Pickerd et al. (2016) explored the failure mechanisms of welded steel containers subjected to internal explosions in air, identifying correlations between weld rupture and overall structural deformation. Fei et al. (2025) performed targeted experimental and numerical investigations on internal explosions in thin-walled sealed steel boxes underwater, focusing on load characteristics and damage responses in confined submerged conditions.

In terms of explosion load transmission and damage evolution in multi-cabin structures, box-type structures in practical engineering contexts are typically arranged as multi-compartment systems. The damage mechanisms affecting adjacent cabins differ from those observed in single sealed compartments subjected to internal explosions. Yao et al. (2023) analyzed the dynamic response and failure behavior of multi-box structures under internal blast loads in air through combined experimental and numerical approaches, focusing on damage features and response characteristics. Wang et al. (2024) developed a double-cabin model to investigate the transmission of explosion-induced dynamic responses between adjacent compartments in an air environment. Li et al. (2019) numerically examined the dynamic response of liquid tanks subjected to internal explosions in air, analyzing pressure distributions and deformation mechanisms of the front and rear plates. Jin et al. (2019) studied the coupled effects of shock waves and fragments on structural damage in liquid tanks under internal explosion conditions in air.

Overall, existing studies have predominantly concentrated on the damage and failure behavior of submerged box structures subjected to external contact or near-field explosions, along with the effects of internal explosions within cabin structures in air. Research addressing the damage mechanisms associated with internal explosions in water-filled wreck compartments and their impact on adjacent cabin structures remains limited. The incompressibility of water and the influence of underwater explosion bubbles introduce notable differences in damage mechanisms, failure patterns,

and dynamic structural responses of adjacent cabins under such conditions. Investigation of internal explosion effects within submerged box structures on neighboring compartments provides both a theoretical basis for wreck dismantling and salvage operations and a deeper understanding of damage mechanisms in submerged multi-cabin systems under realistic conditions.

This study adopts an integrated experimental and numerical simulation methodology to examine the transmission characteristics of internal explosion loads from a central cabin to adjacent compartments, as well as the dynamic response of adjacent bulkhead plates under fully water-filled conditions in a three-cabin steel box. Internal explosion experiments conducted under three distinct conditions yield deformation and damage characteristics of adjacent cabins with varying charge masses and wall thicknesses. Measurements of free-field pressure and surface strain within the structure are obtained to support parameter calibration in the numerical model. Calculations based on the validated model are used to analyze the propagation behavior of internal explosion loads, pressure distribution within cabins, bubble evolution processes, and structural dynamic responses. The study further evaluates the damage patterns and influencing factors associated with internal explosions in adjacent cabins under different charge masses and wall thicknesses, thereby clarifying the damage mechanisms of internal explosions in submerged thin-walled steel box structures. The results offer practical reference for the removal of wreckage obstacles in navigational waterways.

2 Experimental Research

2.1 Structural design of the three-cabin box

A simplified small-scale steel box was developed as the experimental model based on the internal compartment configuration of a representative vessel. The structure consists of three compartments, identified as the front cabin (C1), the central cabin (C2), and the rear cabin (C3), where C1 and C3 are collectively defined as the adjacent cabins. Along the *z*-axis (height), the box includes a top plate and a bottom plate; along the *x*-axis (length), it comprises left and right side plates; and along the *y*-axis (width), it incorporates a front outer plate, front inner plate, rear inner plate, and rear outer plate, as depicted in Figure 1. The overall dimensions of the structure are 140 × 110 × 70 cm in length, width, and height, respectively, while the widths of the three compartments are 20, 70, and 20 cm.

Each compartment is assembled through the welding of steel plates. The top plate, bottom plate, and side plates are each constructed by welding three separate steel plates rather than forming a single continuous plate. Three openings are positioned along the longitudinal centerline of the top plate of the central cabin, intended for explosive charge placement and pressure sensor installation. Two additional openings are located at the centers of the top plates of the front and rear cabins for pressure sensor installation and water filling. The diameter of the opening for charge placement is 8 cm, whereas the openings designated for pressure sensors have a diameter of 3 cm, as illustrated in Figure 2.

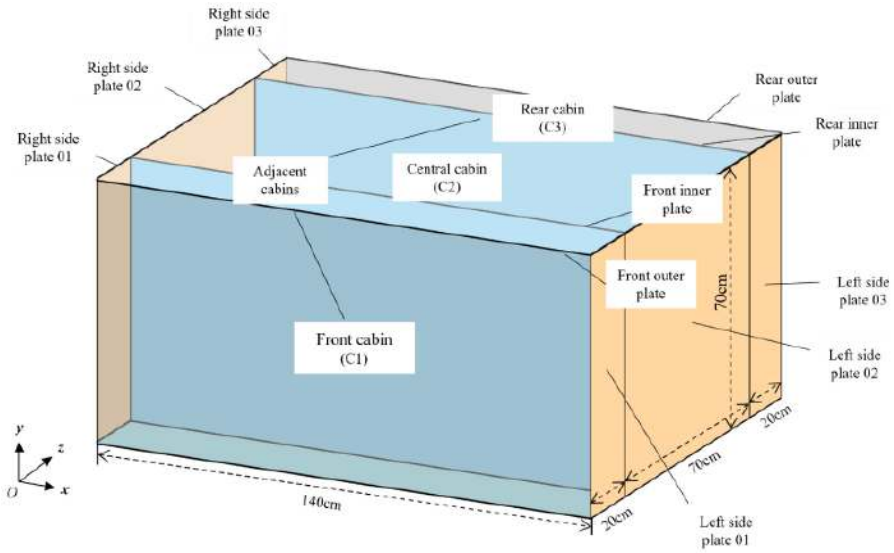


Figure 1: Schematic diagram of the overall experimental model.

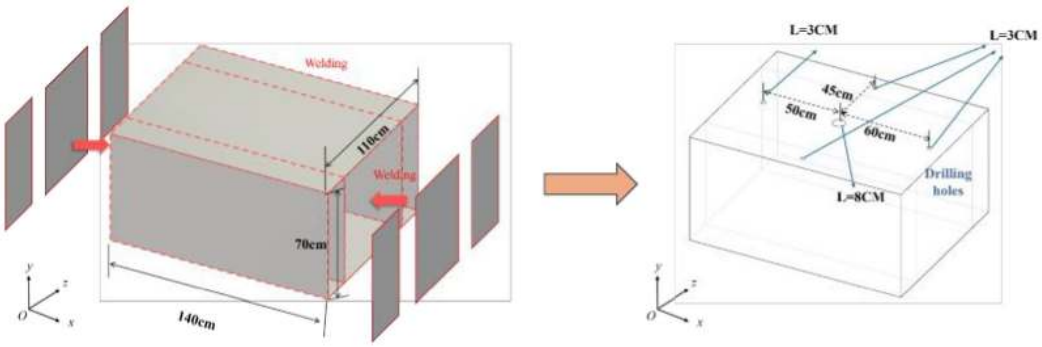


Figure 2: Detailed structural diagram of the test model.

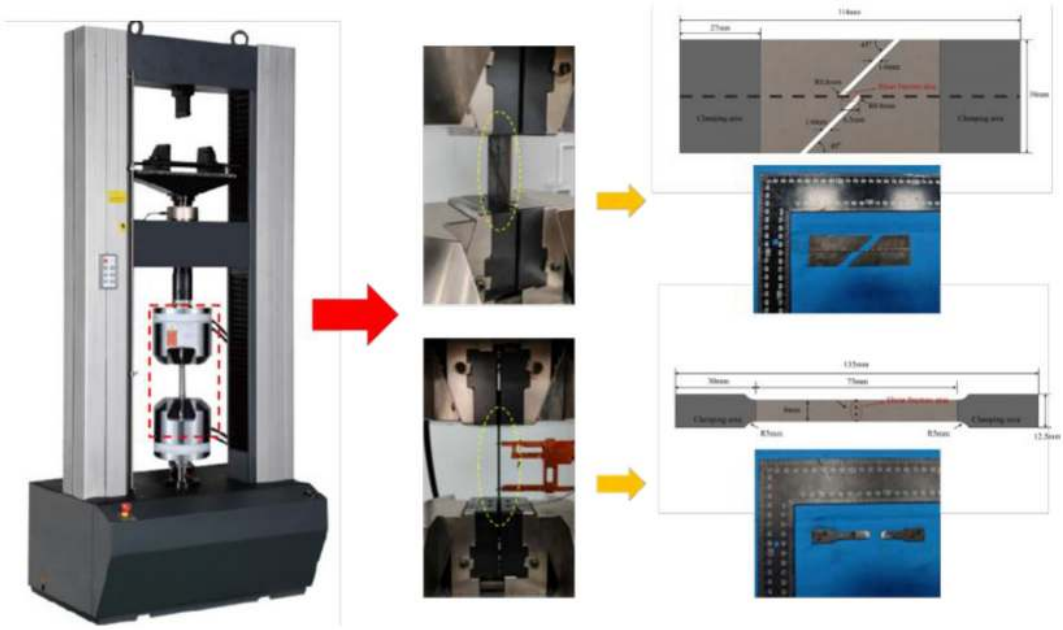


Figure 3: Quasi-static tensile and shear tests.

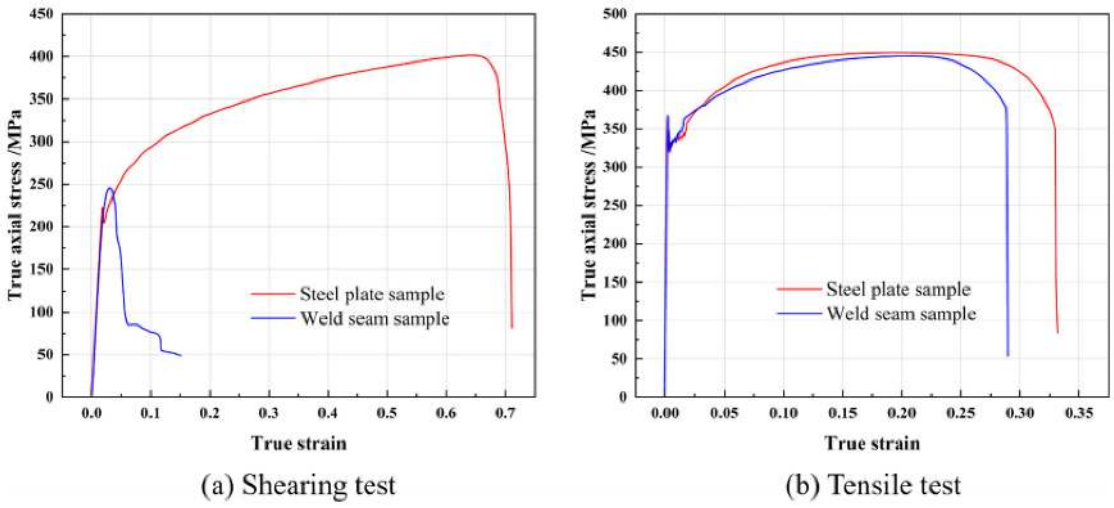


Figure 4: True stress-strain curves of Q235 steel plate and laser-welded joint specimens under tension and shear.

Uniaxial tensile and shear experiments were performed on Q235 steel plate specimens from the same batch, together with small specimens of laser-welded joints, using a computer-controlled electronic universal testing machine to evaluate their tensile and shear failure strengths. As illustrated in Figure 3, the resulting true stress-strain relationships for the Q235 steel plate and the laser-welded joint specimens are provided in Figure 4, and the corresponding experimental data are listed in Table 1.

Table 1. Experimental test results of Q235 steel plate and laser-welded joint specimens

Test specimen	Item	Result	Unit	Test method
Q235 steel plate specimen	Shear force	5.16	kN	HB 6736-93
	Shear strength	402	MPa	
	Tensile strength	450	MPa	GB/Test-228.1-2021
	Elongation after fracture	30	%	
Q235 steel plate laser-welded joint specimen	Shear force	3.21	kN	HB 6736-93
	Shear strength	245	MPa	
	Tensile strength	445	MPa	GB/Test-228.1-2021
	Elongation after fracture	21.5	%	

2.2 Test setup

Cylindrical trinitrotoluene (TNT) charges with a length-to-diameter ratio of 1:1 and a density of 1.6 g/cm^3 were utilized in the experiment, with initiation applied from the top using a No. 8 detonator. Three experimental trials were performed, and the corresponding test parameters are provided in Table 2.

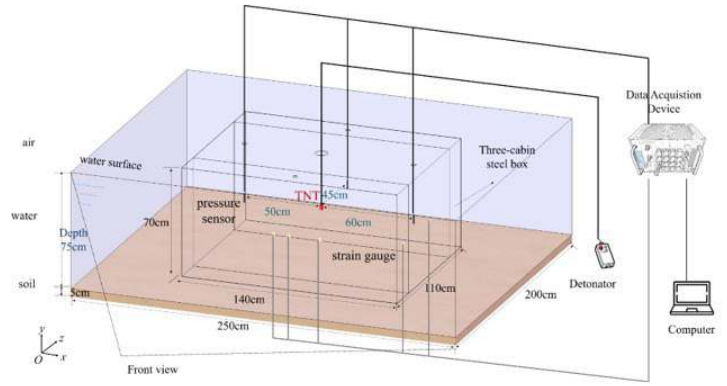
Table 2. Design schemes for different working conditions

Test ID	Charge type	Mass/g	Diameter/mm	Height/mm	Thickness/mm	Relative position
Test-1	Cylindrical TNT charge	20	25	25	1	Center of the central cabin
Test-2	Cylindrical TNT charge	20	25	25	3	Center of the central cabin
Test-3	Cylindrical TNT charge	270	60	60	3	Center of the central cabin

The configuration of the experimental system and the arrangement of the test site are presented in Figure 5. All experiments were conducted within an explosion water tank measuring 250 × 200 × 150 cm. A soil layer of 5 cm thickness was placed at the base of the tank to mitigate the impact of the steel box following detonation. The steel box was installed at the bottom of the tank before completing the assembly of the experimental setup. After securing the box, water was introduced into the tank until the water level extended 5 cm above the top surface of the steel box. At the same time, pre-designed openings were used to ensure complete water filling of the front cabin, central cabin, and rear cabin. The full experimental system consisted of the explosion water tank, the three-cabin steel box structure, the explosive charge and detonator, a synchronized initiation system, a signal conditioning unit, and a data acquisition system.

During the experiment, the explosive charge was introduced into the central region of the steel box through the designated charge opening using a slender rope in combination with a rigid tube, while a counterweight attached at the lower end ensured positional stability. Two pressure sensors were installed within the central cabin through openings of 3 cm in diameter. One of these sensors was also stabilized by a bottom-suspended counterweight and arranged horizontally at the same level as the center of the explosive charge. The sampling frequency was set to 1 MHz. The sensor located at a distance of 50 cm from the charge was denoted as P1, whereas the sensor positioned 60 cm from the charge was denoted as P2, the sensor located at the center of the adjacent cabin, at a distance of 45 cm from the charge, was denoted as P3, as illustrated in Figure 6.

Five strain gauges were installed on the outer surface of the steel box, with a sampling frequency of 20 kHz. The strain gauge positioned at the geometric center of the front outer plate, observed from the front view, was defined as S1. The gauge located 20 cm to the left of S1 was defined as S2, while the gauge placed 10 cm to the right of S1 was defined as S3. On the left side plate, the strain gauge situated at the center of the central cabin region was designated as S4, whereas the gauge located 45 cm to the left of S4, corresponding to the center of the front cabin, was designated as S5. Detailed arrangements are illustrated in Figure 7.



(a) Schematic diagram of the test setup



(b) Photograph of the underwater internal explosion test

Figure 5: Experimental setup and test process

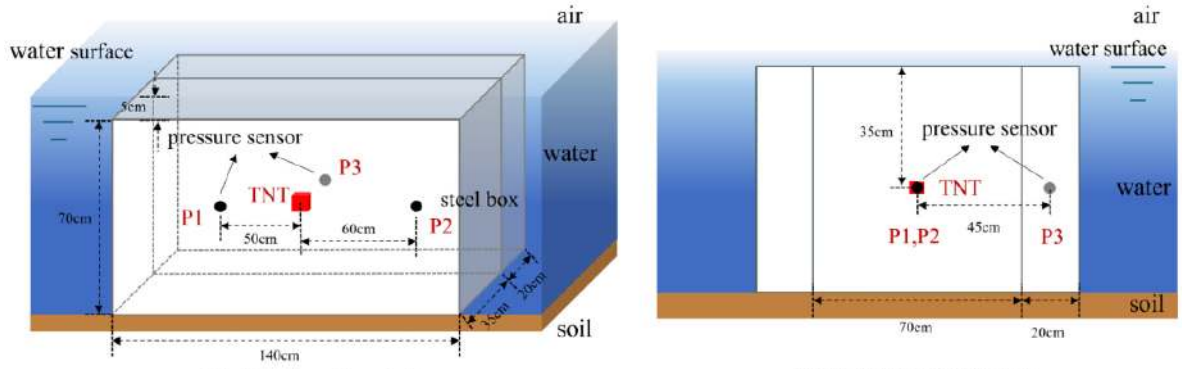


Figure 6: Locations of pressure sensors in the test model

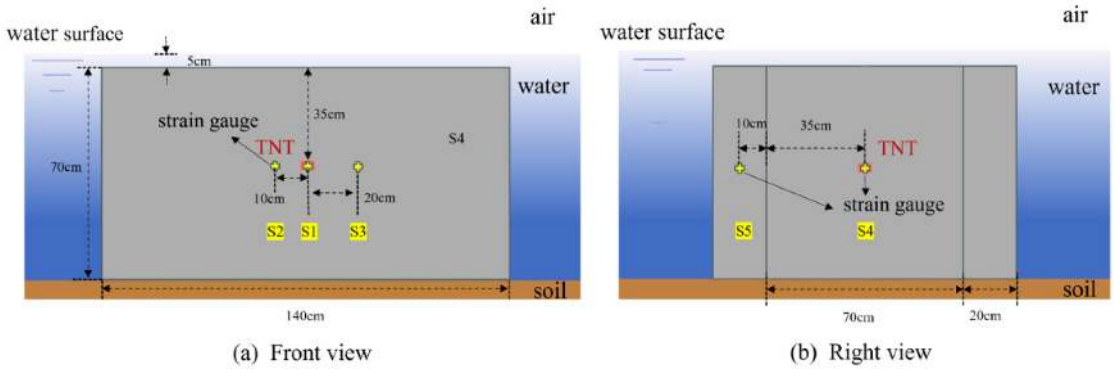


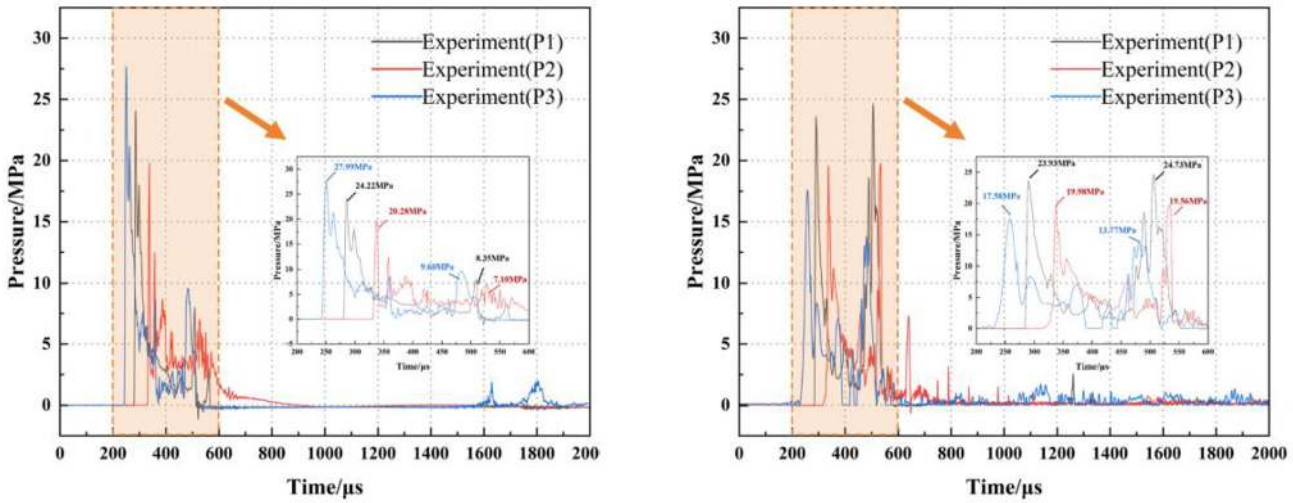
Figure 7: Locations of strain measurement points in the test model

2.3Test results and analysis

2.3.1. Explosion pressure results and analysis

Figure 8 shows the pressure–time histories measured at different locations during the underwater internal explosion in the steel box for Test-1 and Test-2. The results indicate that the pressures in both the central cabin and the adjacent cabins exhibit multiple shock wave peaks in the initial stage of the explosion, followed by several lower-amplitude pressure peaks at later times. The duration of positive pressure is significantly longer than that typically observed in free-field explosion conditions. The presence of multiple shock wave peaks is mainly caused by the superposition of incident or transmitted shock waves at each measurement location, together with repeated reflections from the surrounding boundaries. The later-stage pressure response is primarily governed by shock wave attenuation and bubble pulsation effects.

Under the Test-1 condition, the distances from the detonation center to the measurement points P1, P2, and P3 are 50, 60, and 45 cm, respectively, with corresponding peak pressures of 24.22, 20.28, and 27.99 MPa. Under the Test-2 condition, the peak pressures at these locations are 23.93, 19.98, and 17.58 MPa, respectively. A notable observation is that the peak pressure at P3 is lower than that at P1, even though P3 is closer to the detonation center. This behavior is attributed to the greater attenuation of the transmitted shock wave by the thicker bulkhead before reaching P3 in the adjacent cabin, indicating that wall thickness plays a significant role in reducing shock wave transmission. In addition, the secondary pressure peaks recorded at all three measurement points in Test-2 are markedly higher than those in Test-1, suggesting that increased wall thickness enhances the magnitude of reflected wave pressures within the enclosed structure.



(a) Pressure time-history curves inside the steel box for Test-1

(b) Pressure time-history curves inside the steel box for Test-2

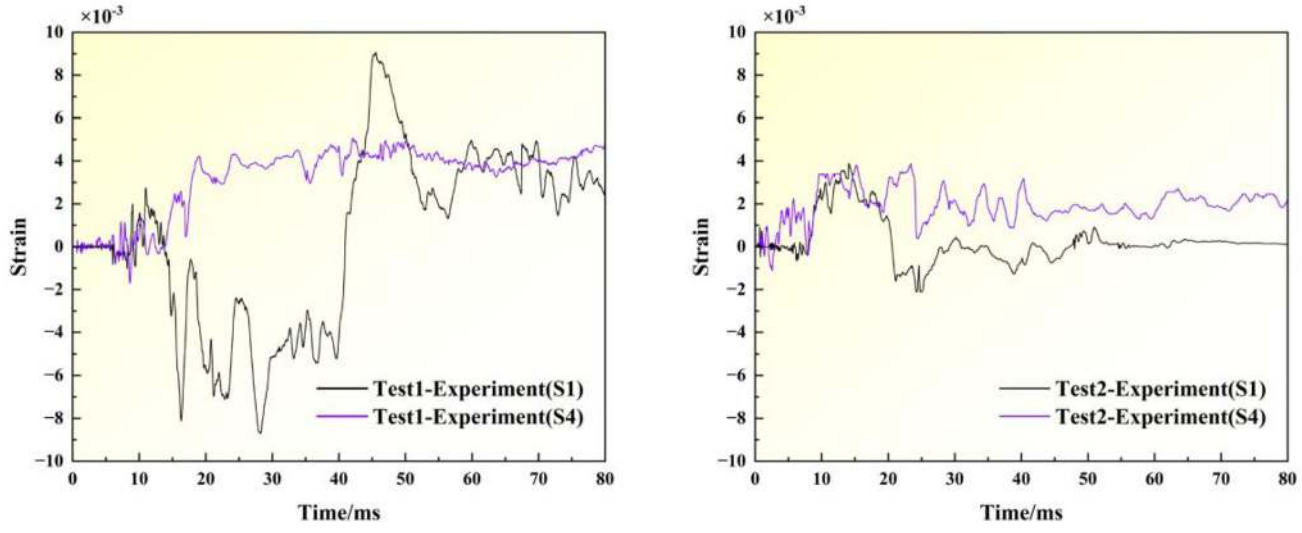
Figure 8: Pressure time-history curves at test measurement points

2.3.2. Strain results and analysis

Figure 9 presents the strain response obtained from the internal explosion tests of the steel box under Test-1 and Test-2 conditions. Strain gauges S1 and S4 were used to record the strain evolution at the center of the front outer plate and the side plate, respectively. The corresponding strain–time histories for both test conditions are shown in Figures 9(a) and 9(b). The results reveal the following:

(i) Under internal blast loading within the steel box, the strain response of the front outer plate follows a characteristic pattern consisting of a rapid initial increase, a gradual decrease, a secondary pronounced increase, and a final stabilization after recovery. In Test-2, the strain at measurement point S1 located at the center of the front outer plate increased sharply at 0.3 ms, followed by a slow decline. A secondary increase then occurred, reaching a peak value of 4.01×10^{-3} ε between approximately 8 and 17 ms, after which it decreased to -2.10×10^{-3} ε and eventually stabilized at 1.87×10^{-3} ε. When interpreted together with the pressure results from Test-2, the initial rapid rise is attributed to the shock wave loading, the subsequent gradual reduction is associated with the attenuation of multiple reflected shock waves within the adjacent cabin, the secondary pronounced increase between approximately 8 and 17 ms is induced by bubble expansion, and the final recovery and stabilization correspond to the bubble contraction stage. (ii) The peak

strains at measurement point S1 in Test-2 during the shock wave phase and the bubble expansion phase are 8.37×10^{-4} ε and 4.01×10^{-3} ε, respectively, the latter being approximately 4.8 times the former. In both tests, the peak strain developed during the bubble expansion phase is markedly greater than that during the shock wave phase, which confirms that the deformation induced by bubble expansion is substantially larger in magnitude than that produced by shock wave loading. (iii) The strain response at measurement point S4 on the side plate shows a distinct pattern, where the recovery magnitude after the substantial increase caused by bubble expansion is smaller, and the stabilized strain level is slightly higher than that observed in the front outer plate. This behavior is mainly related to the reduced structural span of the side plate. (iv) The strain response in Test-1 is notably higher than that in Test-2, indicating that increased wall thickness in the steel box structure enhances resistance to deformation.



(a) Strain time-history curves of the steel box for Test-1

(b) Strain time-history curves of the steel box for Test-2

Figure 9: Strain time-history curves at test measurement points

2.3.3. Damage results and analysis

The damage outcomes of the steel box under Test-1 are illustrated in Figure 10(a). The 1-mm-thick steel box exhibited substantial outward bulging deformation globally. Severe tearing occurred at the weld joint between the top plate and left side plate of the central cabin, and partial tearing was observed at the connections between the top plates and inner plates of both front and rear cabins. Such tearing failure is mainly attributed to structural tensile deformation, where initial failure takes place at the relatively weaker welded joints.

The crack at the weld of the central cabin top plate and left side plate reached 28.5 cm in width. No cracking was detected at the joints of front/rear cabin top plates to the left side plate, nor at the welds connecting front/rear cabin top plates to front/rear outer plates. The crack length at the front cabin top plate–front inner plate joint was 27 cm, while that at the rear cabin counterpart was 18 cm. All joints between cabin top plates and the right side plate remained intact. The measured deflections of front and rear outer plates were 22.5 cm and 13 cm, and those of left and right side plates were 10 cm and 12.5 cm, respectively.

The damage results of the steel box under Test-2 are presented in Figure 10(b). The 3-mm-thick steel box showed relatively limited overall deformation, with plastic deformation of varying intensity along the structural perimeter. Localized cracking occurred at the weld between the top plate and front outer plate with a length of 17 cm; partial cracking was also found at the right side plate–bottom plate joint, and no other prominent cracks were identified.

Distinct plastic hinge line features appeared on the front/rear outer plates, top plate and other wall panels. The central cabin top plate and left/right side plates underwent upward bulging deformation: trapezoidal plastic hinge lines formed on both sides of the top plate and the upper regions of corresponding side plates, and circular plastic hinge lines emerged at the centers of front and rear outer plates. The deflection of the central cabin top plate reached 5.9 cm; deflections of front and rear outer plates were 3.4 cm and 3.3 cm, and those of left and right side plates were 3.0 cm and 3.4 cm, respectively.

The damage results of the steel box under Test-3 are presented in Figure 10(c). Under explosive loading, the top plate, side plates and outer plates of the steel box suffered fragmentation and rupture, causing the front and rear cabins to separate from the central cabin. The front cabin top plate was completely ejected together with the central cabin top plate; the rear cabin top plate fractured fully and remained only partially connected to the central cabin top plate. Significant bending deformation occurred in the top plate, with well-defined plastic hinge lines forming in its central region.

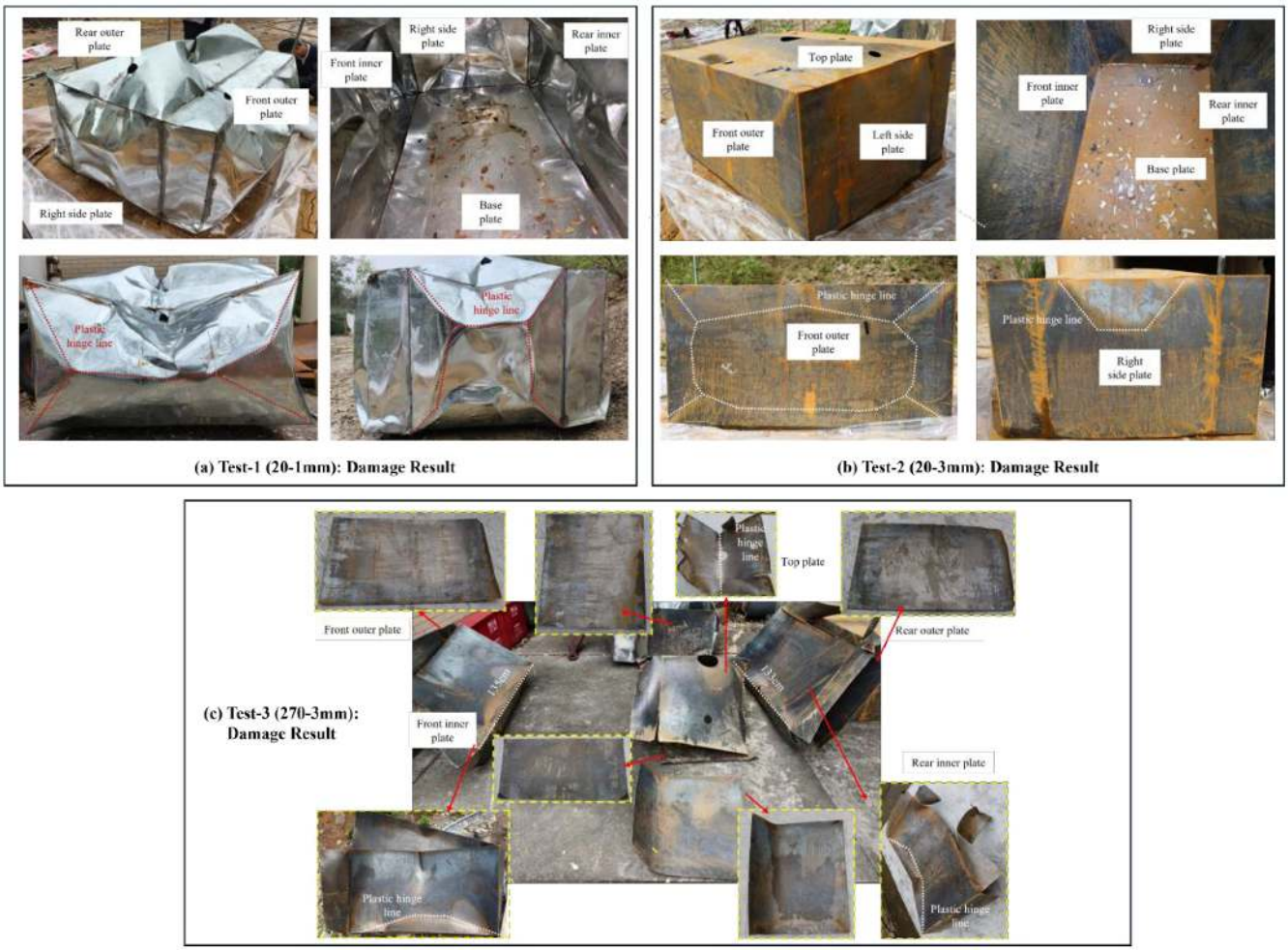


Figure 10: Damage results of Test-1,2,3

A comparative analysis of the damage responses indicates the following observations.

(i) An increase in charge mass leads to a marked escalation in structural damage for a steel box of identical thickness. Considering the 3-mm three-cabin steel box as an example, under a 20-g charge, only minor deformation and localized tearing occurred at edges and corners without structural disintegration. When the charge mass was increased to 270 g, complete disintegration of the central cabin was observed, accompanied by separation of the outer plates.

(ii) For cases with different wall thicknesses, the 1-mm-thick steel box subjected to a 20-g charge exhibited significantly greater outward bulging than the 3-mm-thick configuration. This behavior demonstrates that increased wall thickness effectively reduces the severity of damage induced by internal explosions within the steel box.

(iii) Under a 20-g internal explosion, initial failure occurred at weld locations on the side plates located farther from the charge center. The release of energy through these initial failure regions subsequently alleviated loading intensity in other regions of the steel box, thereby reducing the extent of damage in the remaining structural components.

2.3.4. Experimental conclusions

Internal explosion tests were carried out on a submerged three-cabin box structure. Free-field pressure data, surface strain responses within the box, and the resulting structural damage patterns were obtained and analyzed. The main conclusions are as follows:

1. After detonation of the centrally located charge in the central cabin of the submerged thin-walled three-cabin steel box, the pressure response in both the central and adjacent cabins is characterized by multiple peaks and an extended positive pressure duration. The first pressure peak measured in the central cabin corresponds to the direct incident shock wave, whereas the initial peak recorded in the adjacent cabins is generated by the transmitted wave propagating through the inner plate. Subsequent pressure peaks arise from the superposition of multiple reflections of the incident or transmitted waves from the surrounding boundaries, together with bubble pulsation effects.
2. Under internal explosion loading, the strain responses of the front outer plate and the side plate result from the combined action of shock waves and bubble dynamics. The deformation induced by bubble expansion is substantially larger in magnitude than that produced by shock wave loading.
3. The damage severity of both the central cabin and adjacent cabins increases significantly with increasing charge mass. For the 1-mm-thick steel box subjected to a 20-g charge, the dominant failure modes include plastic deformation and edge tearing without global structural collapse. When the charge mass increases to 270 g, complete disintegration of the central cabin occurs, and the outer plates are ejected together with the adjacent cabin structures. Structural damage decreases with increasing wall thickness. Under a 20-g charge, the outward bulging deformation of the 1-mm-thick steel box panels is significantly greater than that observed in the 3-mm-thick steel box.

3 Numerical Model and Validation

3.1 Model establishment and material constitutive parameters

In this study, the Smoothed Arbitrary Lagrangian–Eulerian (SALE) structured transient fluid–structure interaction method (Babu, et al., 2018) is adopted for numerical simulation. Compared with the conventional arbitrary Lagrangian–Eulerian formulation, the SALE approach enables automatic generation of orthogonal Arbitrary Lagrangian–Eulerian meshes, thereby mitigating mesh distortion, improving the capability to capture fluid–structure interaction behavior, and enhancing overall computational efficiency.

To reduce computational cost, a half-symmetry three-dimensional finite element model is developed for simulating the underwater internal explosion. The unit system is defined as cm-g-μs. The entire computational domain has dimensions of 2.5 × 1.0 × 1.7 m in length, width, and height, respectively, and consists of five components: explosive charge, air, water, soil, and a half-symmetric three-cabin steel box.

The explosive, air, water, and soil domains are all modeled using multi-material Eulerian elements and are mapped into the SALE mesh using the keyword *INITIAL_VOLUME_FRACTION_GEOMETRY. The steel box is discretized using shell elements, while welded connections between individual plates are modeled using the *CONTACT_AUTOMATIC_SURFACE_TO_SURFACE_TIEBREAK keyword, the contact failure parameters were obtained through the aforementioned weld tensile and shear tests (as presented in Figure 4 and Table 1).

The air and water regions in the model have dimensions of 2.5 × 1.0 × 0.75 m, whereas the soil region measures 2.5 × 1.0 × 0.2 m. The TNT charge is represented as a cylindrical geometry with a height-to-diameter ratio of 1:1, and its base radius is determined based on the specified charge mass for each test condition. The steel box model measures 1.4 × 0.55 × 0.7 m, with wall thickness values set to 3 and 1 mm. The water level is fixed at 75 cm, and the top surface of the steel box is positioned 5 cm below the water surface, consistent with the experimental setup.

Symmetry boundary conditions are imposed on the symmetry plane (the *xoy* plane) to constrain nodal displacements, while all other boundaries are assigned non-reflecting boundary conditions. The finite element model is discretized using a hybrid multi-scale meshing strategy (Wang, et al., 2016). The mesh size of the steel box structure is set to 1 cm, and two layers of elements are used through the wall thickness to accurately capture the damage evolution of the steel box. Given the relatively large scale of the computational model, a graded mesh transition scheme is employed to reduce computational cost and improve efficiency, with element sizes varying from 3 to 30 mm. The overall model configuration and mesh distribution are shown in Figures 11 and 12.

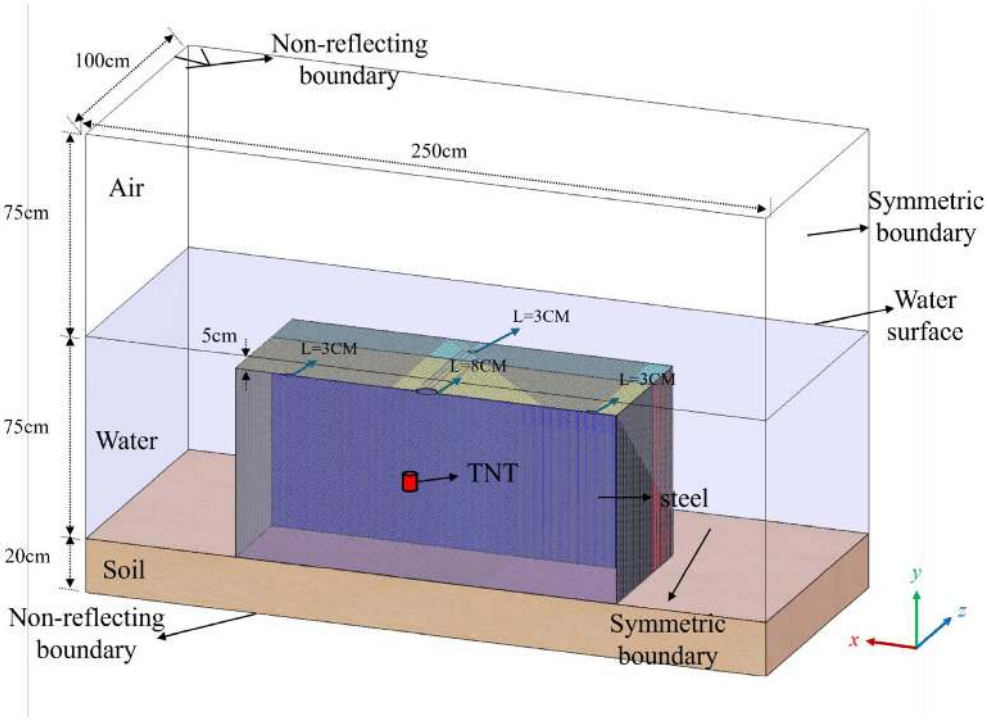


Figure 11: Schematic diagram of the 1/2 finite element model

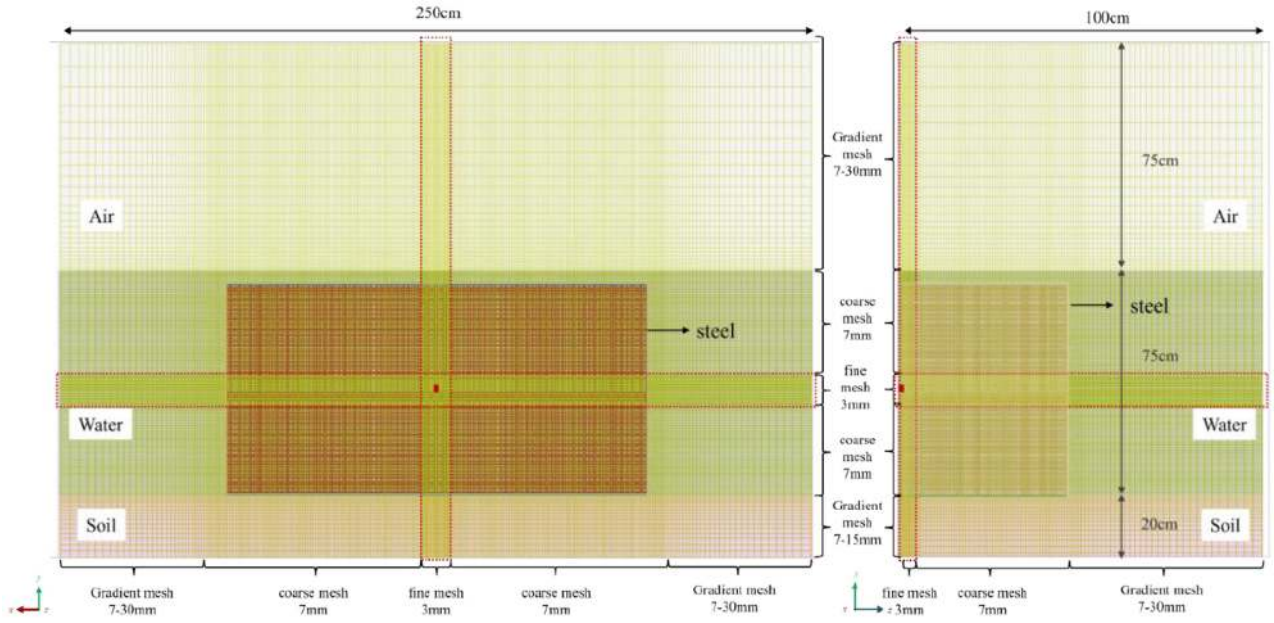


Figure 12: Schematic diagram of the finite element model mesh generation

In the numerical simulation, the explosive material is modeled using *MAT_HIGH_EXPLOSIVE_BURN, while the detonation products are represented through the *EOS_JWL equation of state. The Johes-Wilkins-Lee (JWL) equation of state for TNT is given as follows (Lin, et al., 2024):

$$P = A(1-\frac{\omega}{R_1 V})e^{-R_1 V} + B(1-\frac{\omega}{R_2 V})e^{-R_2 V} + \frac{\omega E_0}{V} \quad (1)$$

For underwater explosion simulations, water is modeled using *MAT_NULL, a void material model with zero yield strength that exhibits fluid-like mechanical behavior. In addition, the physical response of water is described using the *EOS_GRUNEISEN equation of state, whose formulation is expressed as follows (Cheng, et al., 2024):

$$P=\begin{cases}\dfrac{\rho_0 C^2\mu\left[1+\left(1-\dfrac{\gamma_0}{2}\right)\mu-\dfrac{a}{2}\mu^2\right]}{\left[1+\mu-\sum_{i=1}^{3}\dfrac{S_i\mu^i}{(1+\mu)^{i-1}}\right]^2}+(\gamma_0+a\mu)E, & \mu\geq 0\\ \rho_0 C^2\mu+(\gamma_0+a\mu)E, & \mu<0\end{cases} \tag{2}$$

The air medium is also modeled using the same void material formulation (*MAT_NULL) as that applied to water. The corresponding equation of state is defined by the *EOS_LINEAR_POLYNOMIAL model, and its specific expression is given as follows (Cheng, et al., 2024):

$$P=C_0+C_1u+C_2u^2+C_3u^3+(C_4+C_5u+C_6u^2)E \tag{3}$$

Soil is represented using the *MAT_SOIL_AND_FOAM material model, in which the compressive equation of state is approximated through piecewise linear fitting based on ten data pairs. This formulation is commonly used to describe the mechanical response of porous materials, such as soil and foam. The shear modulus, bulk modulus, and plastic yield function constants of the soil are adopted from experimentally calibrated values reported for soil subjected to explosion shock loading (Wang, et al., 2024), ensuring that all the soil parameters fall within physically reasonable ranges.

The steel box material is Q235 steel. In this study, its behavior is described using the *MAT_JOHNSON_COOK constitutive model in combination with the *EOS_GRUNEISEN equation of state (Zhao, et al., 2020). The Johnson–Cook model is expressed as follows:

$$\sigma_y=\left(A+B\varepsilon_p^n\right)\left(1+C\ln\varepsilon^*\right)\left(1-T^{*m}\right) \tag{4}$$

In essence, the Johnson–Cook model represents the combined effects of strain, strain rate, and temperature on the dynamic yield stress in a multiplicative formulation. In this expression, σ_y denotes the yield stress; the initial yield stress of the material under reference strain rate and temperature conditions is represented by A, the strain hardening modulus is denoted by B, and the strain rate sensitivity parameter is represented by C. The dimensionless temperature is defined as Tm= ($T - Troom$)/($Tmelt - Troom$). Considering the influence of weld seams on blast response, the normal failure stress and shear failure stress in the model are specified as 445 and 245 MPa, respectively.

The parameters used in this study are presented in Table 3.

Table 3. Measured deformation and damage data of the steel box under Test-1, 2, 3.

Item		Test-1	Test-2	Test-3
Deflection of plates (cm)	Front outer plate	22.5	3.4	—
	Rear outer plate	13.0	3.3	—
	Left side plate	10.0	3.0	—
	Right side plate	12.5	3.4	—
Overall damage characteristics	Overall deformation	Outward bulging deformation globally	Limited overall deformation	Front and rear cabins separated from the central cabin
	Plastic hinge line	Top plate, outer plate, side plate	Top plate, outer plate, side plate	Top plate, inner plate
	Weld joint	Severe tearing occurred at some weld joint	No obvious cracks at the weld joint	Fragmentation and rupture of the top, side and outer plates

3.2 Mesh sensitivity analysis

To ensure the reliability of the numerical model, a mesh convergence study was performed using different mesh sizes, and the corresponding results are shown in Figure 13. Considering the computational cost, model scale, and overall efficiency, as well as the comparison between the simulated underwater explosion load and the experimental data, a refined mesh size of 3 mm was finally adopted for the fluid domain. The mesh resolutions for the coarser fluid region and the structural domain were selected based on the optimal coupling ratio required by the SALE structured fluid–structure interaction algorithm.

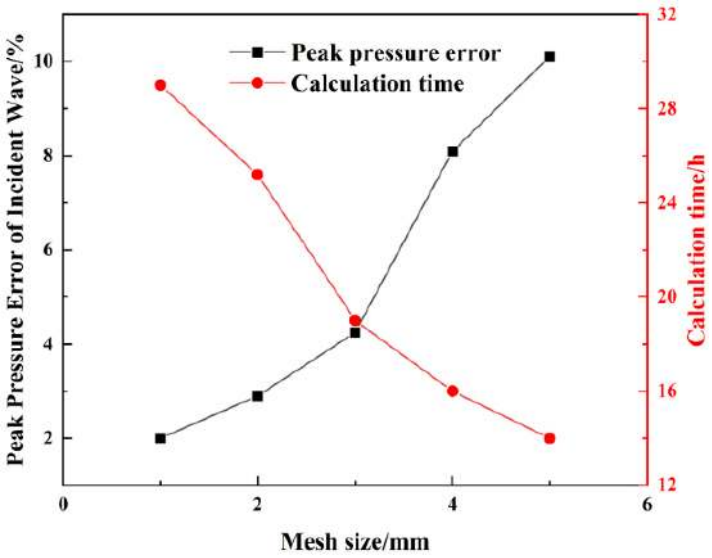


Figure 13: Mesh sensitivity analysis of numerical simulation

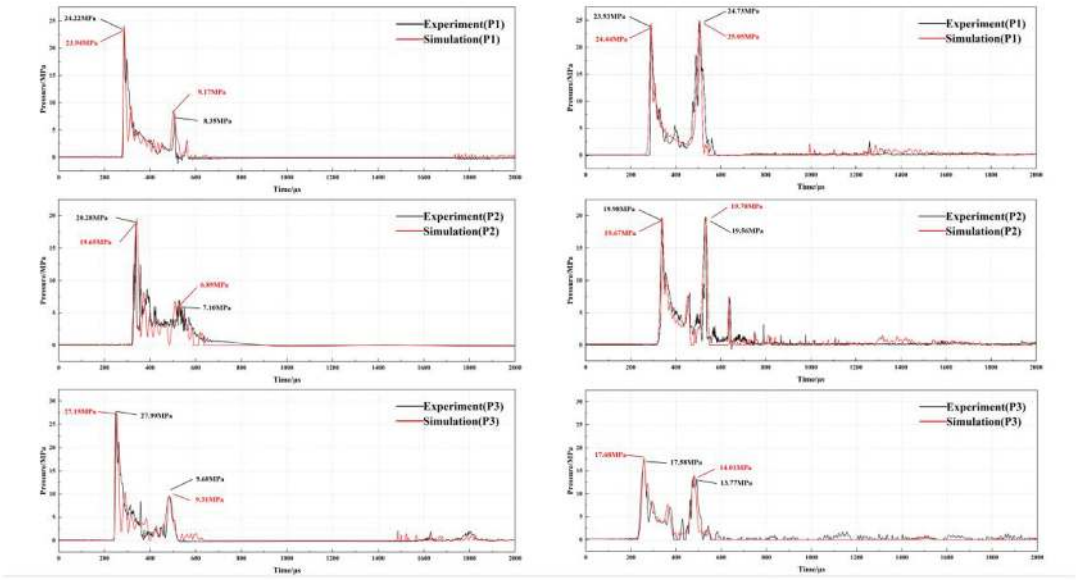
3.3 Numerical model validation

The experimental and numerical shock-wave pressure–time histories for Test-1 and Test-2 are presented in Figs. 14(a) and 14(b), respectively. The peak pressures corresponding to the first incident wave and the second reflected wave at each observation point are summarized in Table 4. A good agreement is observed between the numerical predictions and the experimental measurements, with both the magnitude deviations and the differences in peak arrival times remaining within acceptable ranges. This consistency indicates that the adopted numerical simulation approach is capable of accurately predicting underwater shock-wave loading characteristics.

Table 4. Material parameters

Material	**Material input data**								
TNT	**ρ (g·cm^{-3})**	**D (cm·μs^{-1})**	**A (Mbar)**	**B (Mbar)**	**R1**	**R2**	**ω**	**E (Mbar)**	
	1.6	**0.693**	**3.74**	**0.0323**	**4.15**	**0.95**	**0.3**	**0.07**	
Water	ρ (g·cm^{-3})	C (cm·μs^{-1})	γ	S1	S2	S3	a	E (Mbar)	
	1.0	0.1647	0.35	2.56	1.986	1.2268	0	2.9×10^{6}	
Air	ρ (g·cm^{-3})	C1	C2	C3	C4	C5	C6	E (Mbar)	
	0.00129	0	0	0	0.4	0.4	0	2.5×10^{6}	
Soil	ρ (g·cm^{-3})	G (MPa)	K (MPa)	a0	a1	a2			
	1.73	63.8	3×10^{4}	1.73×10^{12}	7.03×10^{6}	0.3			
Q235	ρ (g·cm^{-3})	E (GPa)	G (GPa)	v	A (MPa)	B (MPa)	n	c	m
	7.83	200	80.8	0.3	370	438	0.6	0.01	0.669

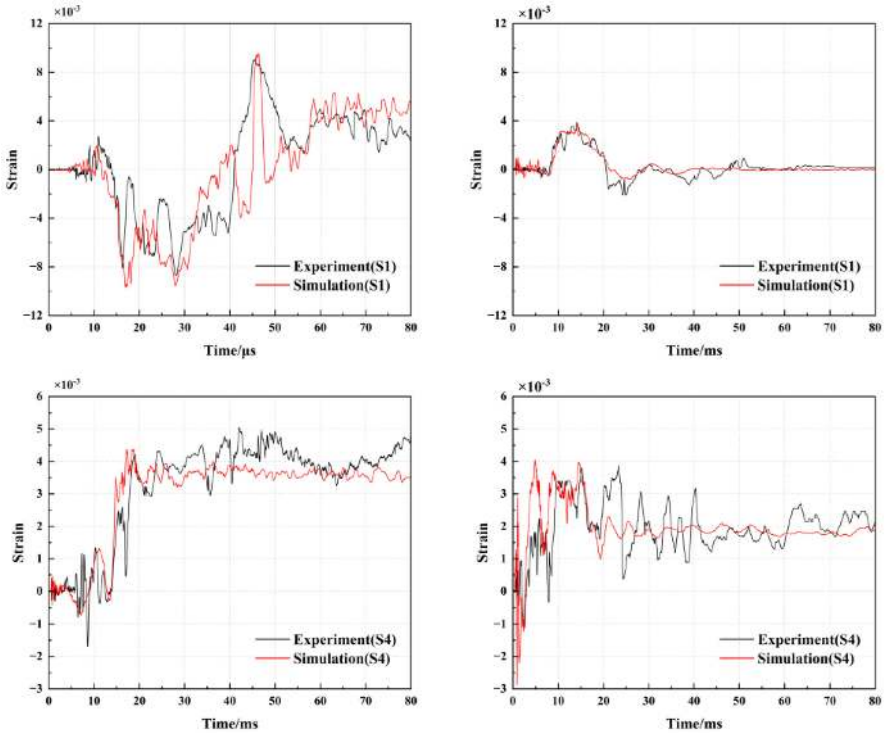
Figure 15(a) compares the strain responses obtained from experiments and numerical simulations at measurement points S2 and S4 under the Test-1 condition, whereas Figure 15(b) presents the corresponding comparison for Test-2. The overall variation trends of the curves show good agreement between numerical predictions and experimental measurements.



(a) Comparison of internal shock wave curves in the steel box for Test-1

(b) Comparison of internal shock wave curves in the steel box for Test-2

Figure 14: Comparison of shock wave pressure time-history curves between experiment and numerical simulation



(a) Comparison of strain curves of the steel box for Test-1

(b) Comparison of strain curves of the steel box for Test-2

Figure 15: Comparison of strain time-history curves between experiment and numerical simulation

The numerical damage patterns for Test-1, Test-2, and Test-3 are shown in Figure 16. Compared with experimental observations, the numerical results for Test-1 and Test-2 demonstrate consistent outward bulging deformation of the wall plates, as well as similar plastic hinge line distributions on the outer plates of the adjacent cabins. Taking Test-2 as an example, the experimentally measured center deflection of the front plate of the steel box is 3.40 cm, while the corresponding numerical result is 3.24 cm. The relative error between the two is 4.71%, which remains within an acceptable range. For the Test-3 numerical simulation, complete disintegration of the central cabin structure is observed, with the outer plates being ejected together with the adjacent cabins, which is consistent with the experimental results. These comparisons confirm that the numerically predicted deflections of the steel box front plate are in good agreement with the experimental measurements.

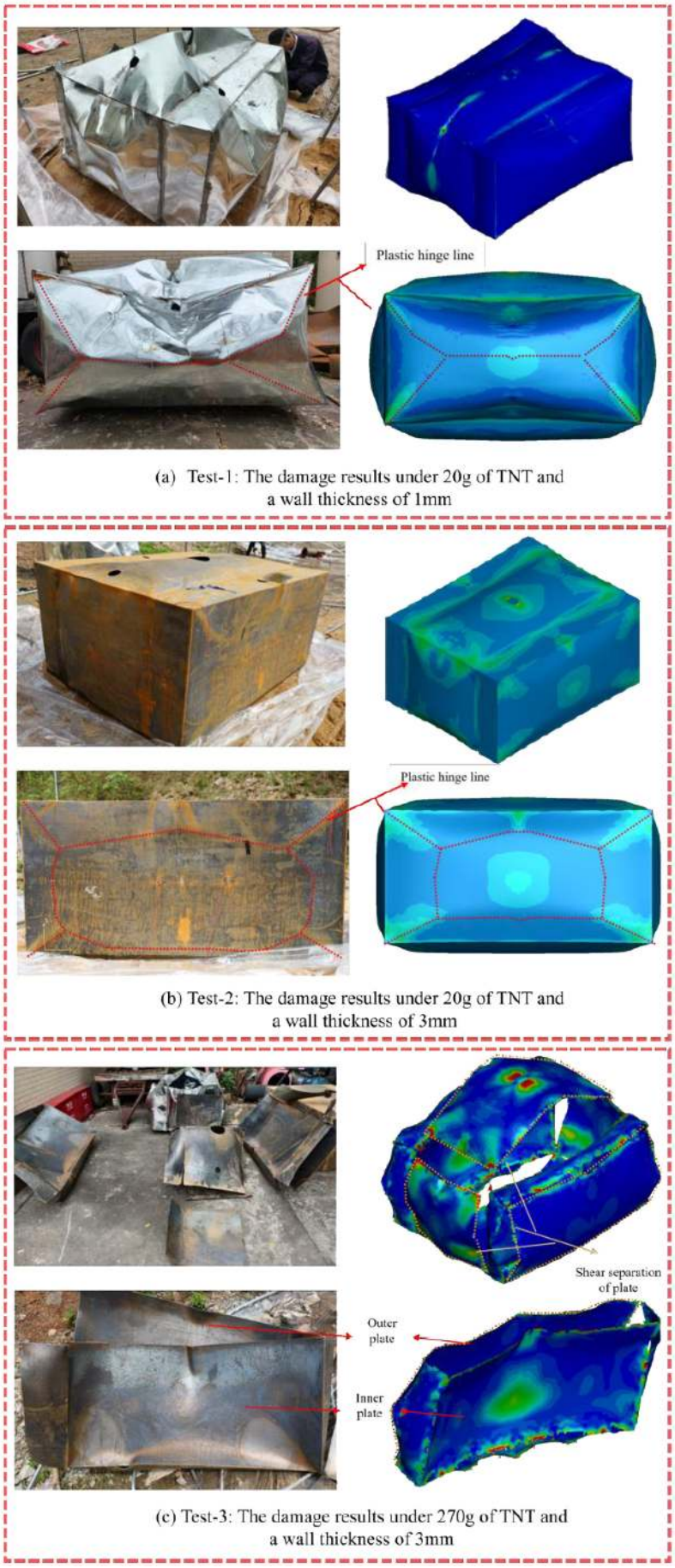


Figure 16: Comparison of damage results between experiment and numerical simulation

4. Dynamic Response of Adjacent Cabin Structures Subjected to Internal Explosion in the Central Cabin

4.1 Explosion shock wave loading in adjacent cabins

Taking Test-2 as an example, Figure 17 illustrates the pressure distribution contours during the shock-wave propagation stage under the Test-2 condition. After detonation of the explosive charge, within 0–175 μs, the spherical shock wave (Incident wave I) generated by the internal explosion propagates radially outward and continuously attenuates. At 175 μs, the shock wave impinges on the walls of the central cabin, resulting in reflection (Reflection wave I) and transmission (Transmitted wave I). At 210 μs, the shock wave transmitted through the top plate reaches the free water surface and is reflected, generating a downward-propagating rarefaction wave. At 380 μs, the first transmitted wave entering the front and rear cabins arrives at the outer plates, where further reflection and transmission occur. Meanwhile, the initial reflected waves from multiple bulkheads within the central cabin converge, forming a second reflected wave (Reflection wave II) in the front and rear adjacent cabins. At 440 μs, the shock wave within the central cabin reaches the side plates, where reflection and transmission processes take place. The reflected waves within the cabin subsequently converge and superimpose before propagating outward. In the front and rear adjacent cabins, the second reflected wave reaches the inner plates, inducing reflection (Transmitted wave IV) and transmission (Reflection wave III). The transmitted and reflected wave components then superimpose within the central cabin and adjacent cabins, respectively, forming localized pressure concentration regions. By 560 μs, after multiple cycles of reflection and superposition, the shock wave exits the box structure, marking the end of the shock-wave action phase.

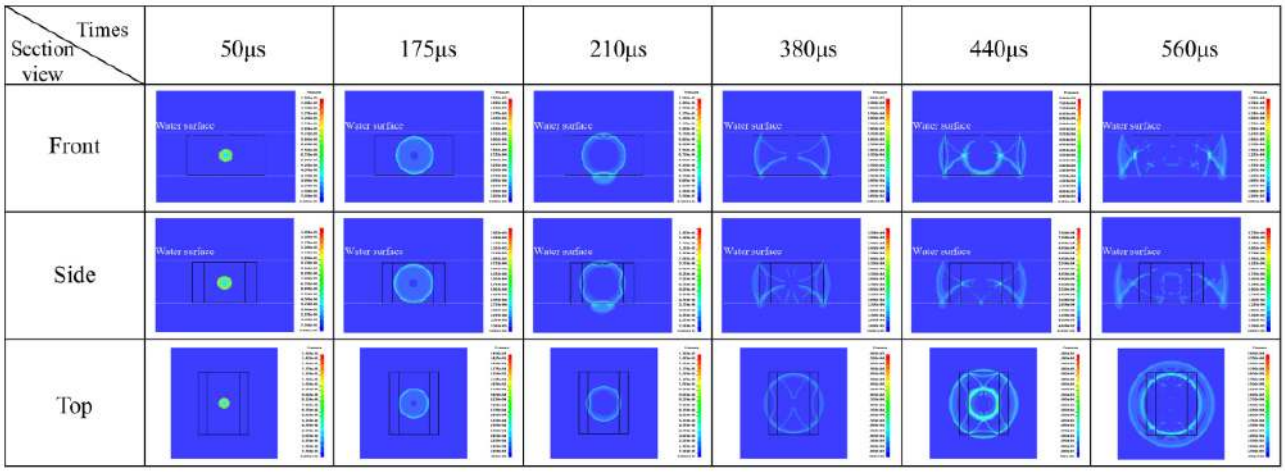


Figure 17: Shock wave pressure contours of the three-compartment steel box under Test-2

Based on the pressure contours, the propagation mechanism of the shock wave generated by the central cabin explosion into the front and rear adjacent cabins, together with its subsequent multiple reflection attenuation within the adjacent cabins, is schematically illustrated in Figure 18. The shock wave observed in the adjacent cabins originates from the transmission of the incident shock wave (Incident wave I) propagating from the central cabin. The transmitted wave within the adjacent cabins is subsequently reflected and focused by the top and bottom plates, outer plates, and side plates, leading to the formation of multiple localized pressure convergence regions and exhibiting multi-peak characteristics. After undergoing repeated reflection and transmission processes within the adjacent cabins, the shock wave pressure peaks decay rapidly.

The physical essence of this propagation process is dominated by the wave impedance regulation of the inner plate and the wave confinement effect of the enclosed adjacent cabins. When an incident shock wave impinges on the inner plate, driven by the impedance mismatch among the water medium in the central cabin, the steel plate, and the water medium in the adjacent cabin, a considerable proportion of wave energy is reflected back to the central cabin, another fraction is dissipated via the plastic deformation of the plate, and only the residual energy is transmitted into the adjacent cabin. The transmitted wave entering the adjacent cabin is subsequently trapped by the enclosed cabin boundaries and undergoes multiple reflections among the outer plate, top and bottom plates, and side plates; such wave confinement and multi-path superposition mechanism also accounts for the formation of local pressure convergence zones near the corners of the adjacent cabin. The wave amplitude is attenuated with each reflection, and the superposition of wave systems propagating along different paths yields a pressure time-history curve with distinct multi-peak characteristics. Accordingly, at the identical standoff distance, the peak pressure amplitude in the adjacent cabin is lower than that in the central cabin during the shock wave phase, accompanied by more peak occurrences and a longer pressure duration.

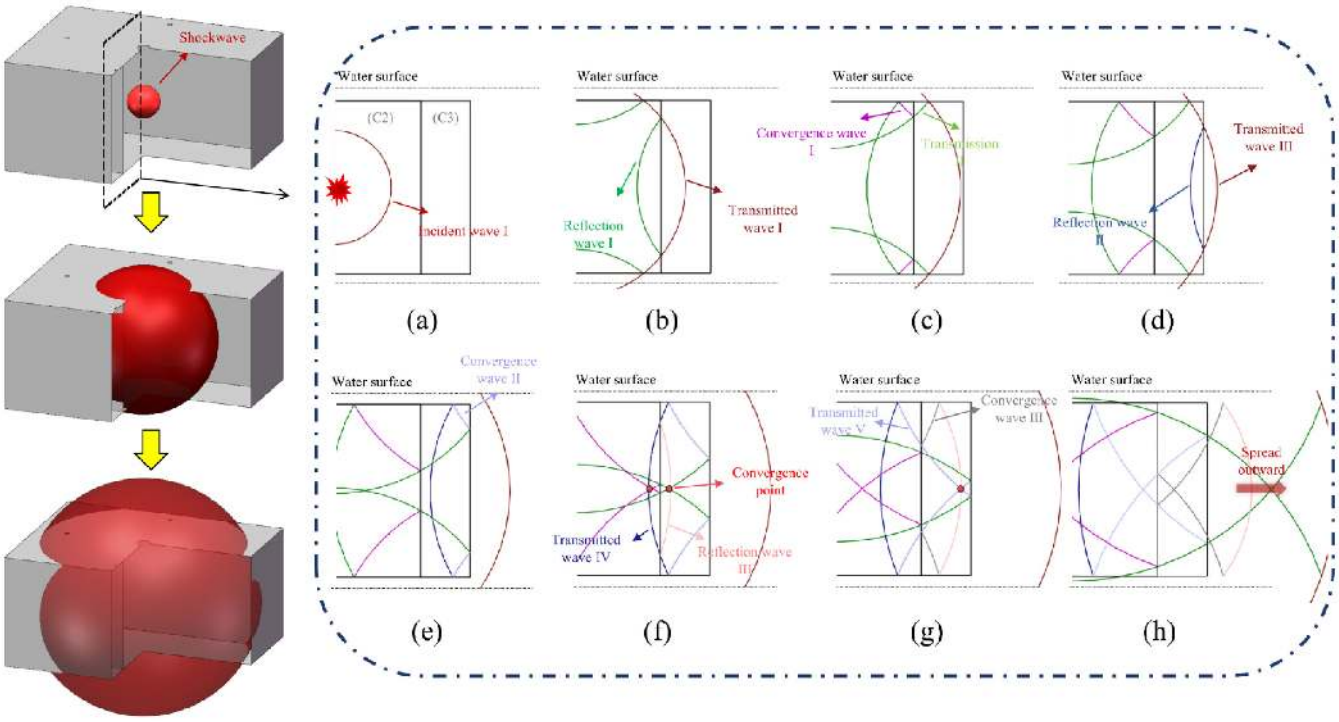


Figure 18: Underwater shock wave propagation process inside the three-compartment steel box

To examine the propagation characteristics and loading effects of the underwater explosion shock wave within the adjacent cabins of the three-cabin structure, measurement points B1–B6 are arranged at 10 cm intervals along the width direction (*z*-axis) of the model. In parallel, measurement points B7–B12 are positioned at equal spacing along the length direction (*x*-axis) within the central cabin, as illustrated in Figure 19. The pressure–time history curves of the shock wave recorded at each measurement point are presented in Figure 20.

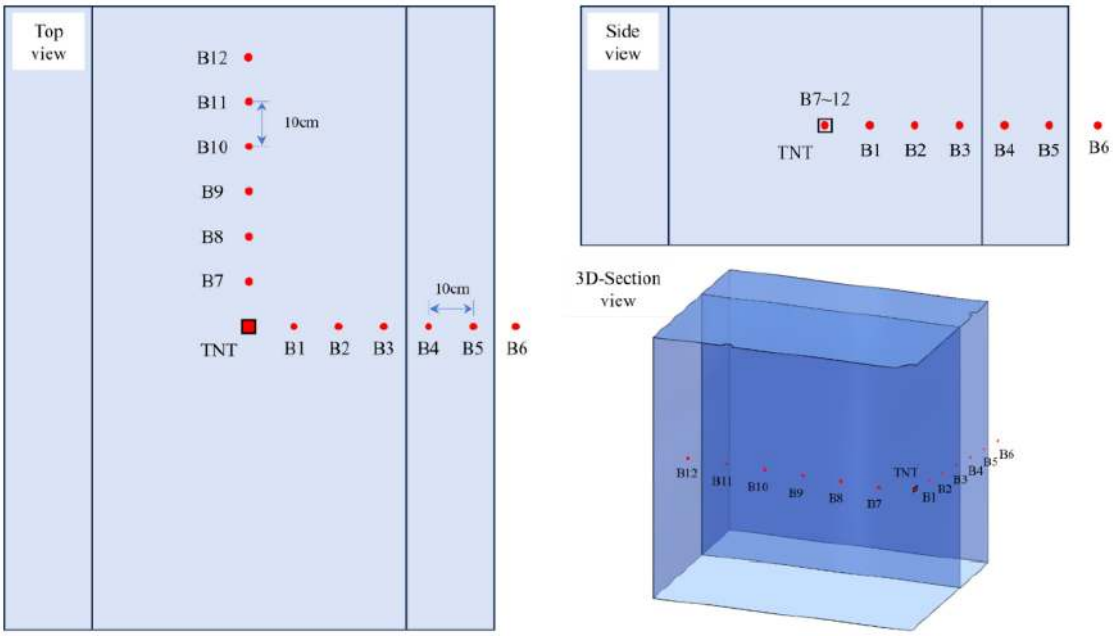


Figure 19: Schematic diagram of internal location selection for the three-compartment steel box

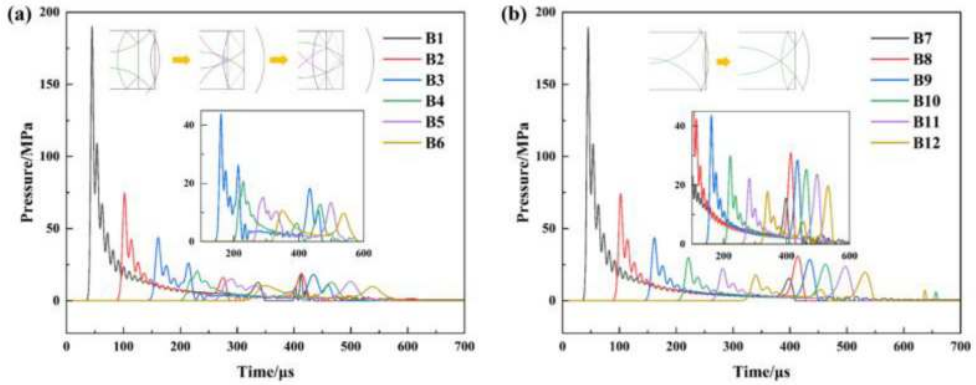


Figure 20: Pressure time-history curves at selected internal points of the three-compartment steel box

Under the Test-2 condition, the pressure–time history curves at measurement points B4–B5 within the adjacent cabins are compared with those at measurement points B9–B10 located at equivalent standoff distances in the central cabin, as well as with the pressure–time response obtained from a numerical simulation with the same charge mass and standoff distance in an infinite water domain (Figure 21). The results indicate the following:

1. The shock wave responses in both the adjacent cabins and the central cabin exhibit multi-peak characteristics. In the central cabin, the first peak corresponds to the incident wave, and its peak magnitude and attenuation behavior are consistent with those observed under free-field conditions, as indicated by label a in the figure. Subsequent peaks arise from the superposition of reflected shock waves from multiple bulkheads; for example, label b corresponds to the convergence of reflections from the front and rear inner plates as well as the top and bottom plates, whereas label c is associated with reflections from the side plates. In the adjacent cabins, the first peak corresponds to the transmitted wave generated as the incident wave from the central cabin propagates through the inner plate, as denoted by label d. The remaining peaks result from the superposition of waves reflected from the boundaries of the adjacent cabins, together with secondary transmitted waves from the central cabin. Label e represents the reflected wave originating from the front plate located 20 cm away, which is the first boundary encountered by the transmitted wave in the adjacent cabin. Label f corresponds to the combined effect of reflections from multiple bulkheads.
2. The overall pressure magnitude at measurement points B4–B5 in the adjacent cabins is significantly lower than that at measurement points B9–B10 in the central cabin for the same standoff distance. The peak pressure of the initial shock wave decreases by 9.26 and 7.25 MPa, respectively, primarily due to rapid attenuation as the wave transmits through the inner plate from the central cabin. The second peak is reduced by 12.55 and 10.30 MPa, respectively, mainly as a consequence of reflection attenuation and the temporal mismatch in wave superposition caused by the geometric configuration of the front and rear cabins.

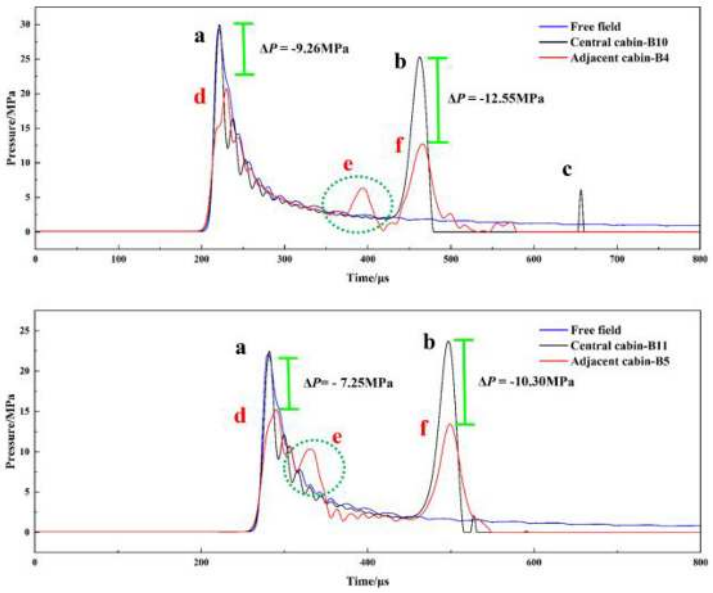


Figure 21: Pressure time-history curves of water elements under different environmental conditions

By comparing measurement points B4 and B10, as well as B5 and B11, under the Test-1, Test-2, and Test-3 conditions, the peak pressure attenuation coefficient α of the underwater shock wave propagating into the adjacent cabin through the inner plate is summarized in Table 5. For a wall thickness of 1 mm, the attenuation coefficient corresponding to the first shock wave is approximately 0.89, whereas for a wall thickness of 3 mm, it is approximately 0.73. The attenuation coefficient α increases with increasing partition plate thickness and shows a slight increase as the intensity of the incident wave decreases.

Table 5. Comparison of peak pressure values between numerical simulation and experiment

Test ID	Measurement point	Peak pressure of incident wave			Peak pressure of reflected wave		
		Experimental value /MPa	Numerical value /MPa	Error /%	Experimental value /MPa	Numerical value /MPa	Error /%
Test-1	P1	24.22	23.94	1.16	8.35	9.17	8.94
	P2	20.28	19.65	3.11	7.10	6.89	2.96
	P3	27.99	27.15	3.00	9.60	9.31	3.02
Test-2	P1	23.93	24.44	2.09	24.73	25.05	1.28
	P2	19.98	19.67	1.55	19.56	19.78	1.11
	P3	17.58	17.68	0.57	13.77	14.01	1.71

4.2 Bubble pulsation characteristics and pressure

The temporal evolution of bubble morphology under the three test conditions is presented in Figure 22. The processes of bubble expansion and contraction predominantly occur within the central cabin where the explosive charge is located. Under Test-1 and Test-2 conditions, bubble expansion compresses the surrounding water medium, leading to outward bulging of the bulkhead plates in the central cabin. In the adjacent cabins, the outer plates also exhibit outward deformation due to the transmission of water compression effects. After reaching its expansion limit within the confined central cabin, the bubble initiates inward contraction. As a result, both the expansion and contraction stages are primarily confined to the central cabin.

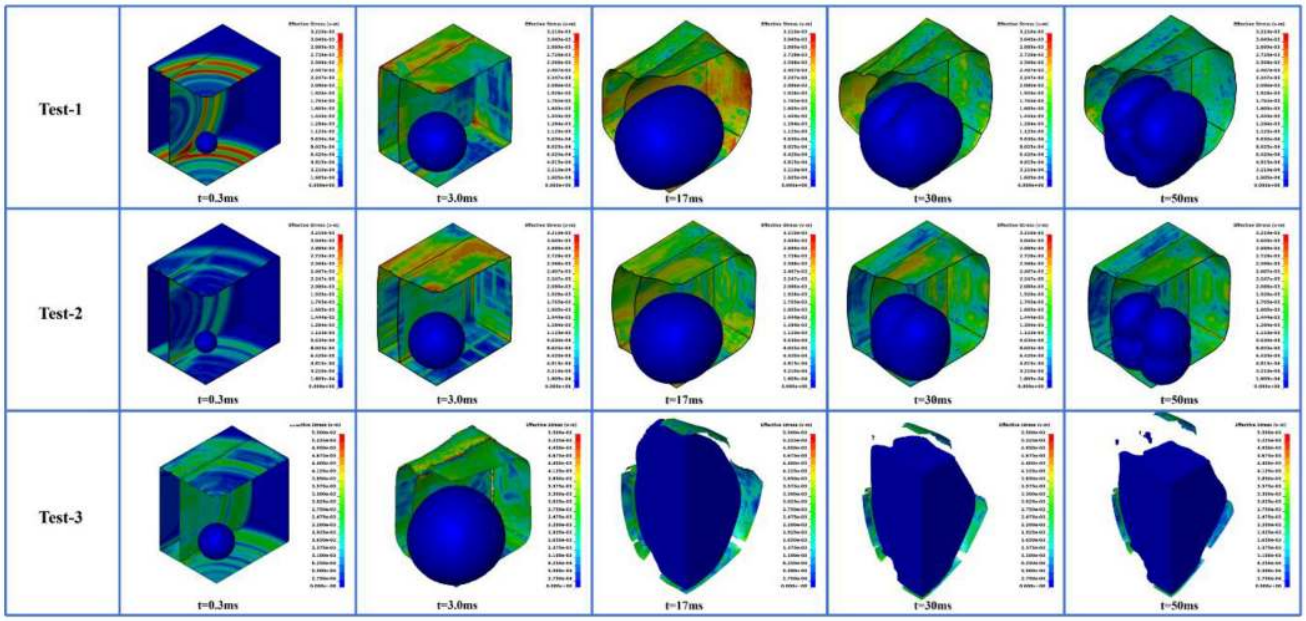


Figure 22: Bubble expansion process under different cases

The detailed bubble morphology evolution for Test-1 is illustrated in Figure 23. Following detonation, the bubble generated within the central cabin expands outward in a nearly spherical form, continuously compressing the surrounding water. At 17.7 ms, the bubble attains its maximum size, forming an approximately ellipsoidal shape with a volume of 45,285 cm^3. Subsequently, contraction begins; at 60 ms, the bubble exhibits a characteristic butterfly-shaped morphology during contraction, and by 80 ms, the central region becomes further indented.

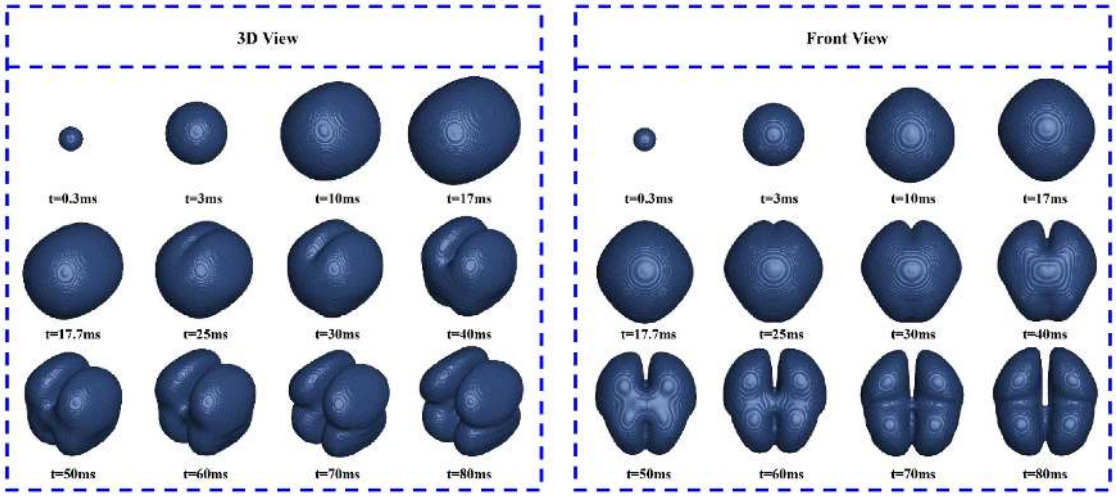


Figure 23: Bubble morphology evolution inside the three-compartment steel box under Test-1

Under Test-3 conditions, the increased charge mass results in a significantly higher bubble expansion velocity. Cracking initiates at plate edges and corner joints under the elevated expansion pressure. The bubble then escapes through these fractured regions, continues expanding externally, and promotes further crack propagation. The central cabin undergoes complete disintegration, and the front and rear adjacent cabins, together with the inner plates, are expelled as an integrated unit. During the expansion phase, the bubble does not penetrate the adjacent cabins.

Under the three test conditions described above, no penetration of the bubble into the adjacent cabins was observed. To further investigate the morphological evolution when a bubble enters an adjacent cabin after rupture of the inner plate, a 270-g cylindrical charge was placed at a distance of 5 cm from the front inner plate within the central cabin and detonated. The resulting bubble morphology as it passes through the opening at the center of the inner plate into the adjacent cabin is presented in Figure 24. The results show that once rupture occurs in the inner plate, the bubble penetrates the adjacent cabin through the opening and compresses the surrounding water medium, leading to an increase in pressure. Subsequently, the high-pressure water in the adjacent cabin flows back into the bubble through the opening in the inner plate. Continuous intrusion of the water medium results in the formation of multiple dispersed gas-water mixture regions within the bubble in the central cabin, while a small portion of the bubble may remain within the adjacent cabin.

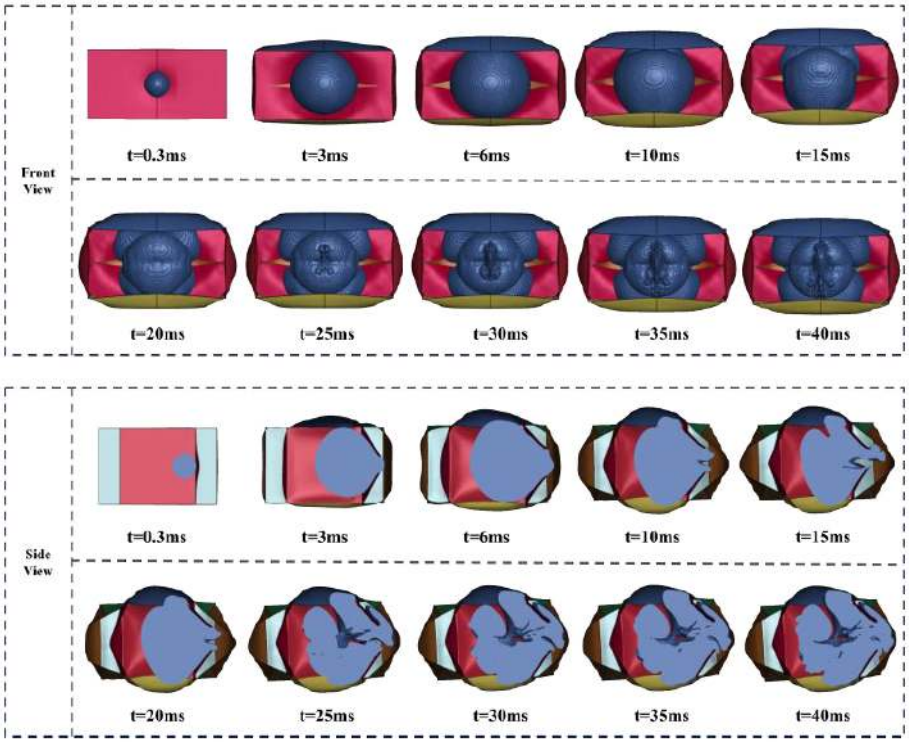


Figure 24: Bubble morphology evolution during the formation of the breach in the inner plate

To further examine the pressure distribution of the flow field within the central and adjacent cabin structures during the bubble pulsation phase, Test-2 is taken as a representative case. Figure 25 presents the pressure contours of the flow field at different time instants under this condition. As illustrated, at 3 ms, the detonation-induced bubble within the central cabin expands outward and continuously compresses the surrounding water medium, resulting in an increase in internal pressure. From 3 to 17 ms, the bubble progressively expands to its maximum radius, while the surrounding water in the central cabin undergoes continuous compression. In the adjacent cabins, pressure increases gradually due to the compression of the water medium induced by the plastic deformation of the inner plates. Between 17 and 30 ms, the over-expanded bubble within the central cabin contracts inward, causing a corresponding reduction in pressure in both the central and adjacent cabins, accompanied by localized rebound at the centers of the outer plates. By 80 ms, the bubble within the central cabin undergoes inward collapse, and the pressure within the adjacent cabins stabilizes at a relatively low level.

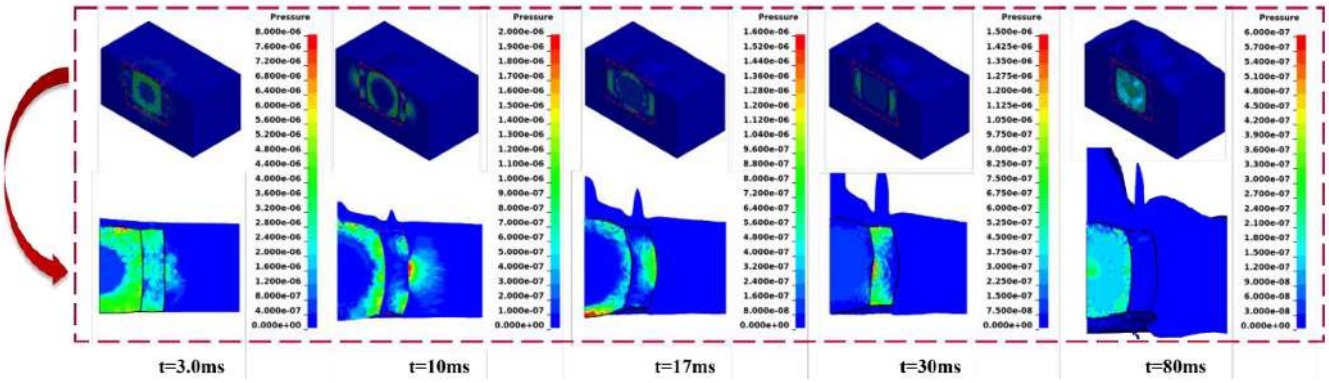


Figure 25: Evolution contours of bubble pressure load inside the three-compartment steel box under Test-2

Figure 26 illustrates the pressure–time histories of water elements at measurement points B10 and B11 in the central cabin, as well as B4 and B5 in the adjacent cabins, during the bubble expansion stage under the Test-2 condition. During the bubble pulsation phase, the pressure responses in both the central and adjacent cabins exhibit relatively low amplitudes with extended durations. The maximum pressures at measurement points B10 and B11 in the central cabin are 0.63 and 0.52 MPa, respectively, whereas the corresponding values at measurement points B4 and B5 in the adjacent cabins are 0.26 and 0.42 MPa. Considering measurement point B5 in the adjacent cabin as an example, the pressure peak at approximately 15 ms reaches 0.52 MPa, which is significantly lower than the peak value of 15.25 MPa recorded during the shock-wave phase. The pressure response associated with the bubble pulsation phase continues to evolve up to 35 ms, whereas the shock-wave-induced pressure effects have essentially dissipated by 800 μs.

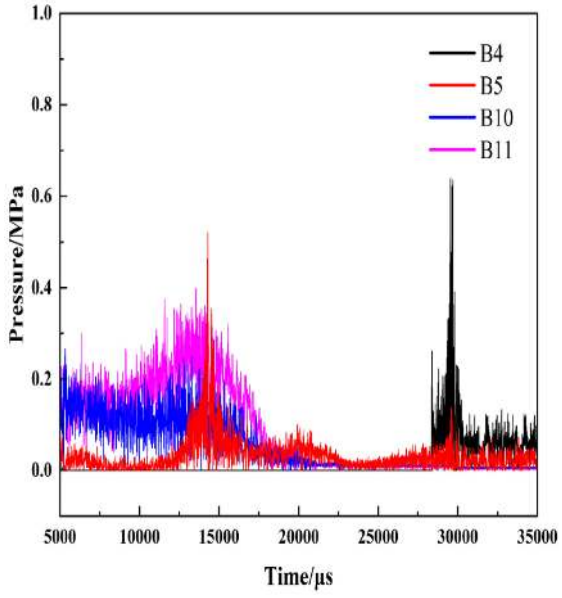


Figure 26: Pressure time-history curves at points B4-5 and B10-11 during the bubble pulsation phase

4.3 Dynamic response of adjacent cabins under explosion loading

The dynamic damage evolution of the central cabin and adjacent cabins under Test-1, Test-2, and Test-3 conditions is compared, as illustrated in Figure 27. After detonation of the charge within the central cabin, the shock wave does not produce significant damage to the inner and outer plates. At 3.0 ms, the free surface exhibits upward bulging, while the expanding bubble compresses the internal water medium, inducing plastic deformation in the bulkhead plates of the central cabin. The deformation of the inner plates leads to pressure variations within the front and rear adjacent cabins. Between 3.0 and 17 ms, continued bubble expansion further amplifies the deformation of the inner plates, resulting in increased pressure within the adjacent cabins and enhanced deformation of the corresponding wall plates. This effect is more evident under the Test-1 condition. Under the Test-3 condition, where a larger charge mass is applied, direct bubble compression causes the inner corners of the central cabin to become more prone to failure than the outer corners. The strain at the corners of the bulkhead plates increases rapidly, leading to cracking and rupture, followed by the onset of separation between the adjacent cabins and the central cabin, along with crack formation at the corners of the outer plates. From 17 to 30 ms, due to bubble contraction, the deformation rate of the bulkhead plates in the central cabin gradually decreases. Under Test-1 and Test-2 conditions, localized rebound occurs on the outer plates of the adjacent cabins, with more pronounced deformation observed in thinner plates. After 30 ms, the deformation of the wall plates under all test conditions essentially stabilizes. Under the Test-3 condition, however, continued bubble expansion causes the adjacent cabins to move outward from the central cabin as an integrated structure.

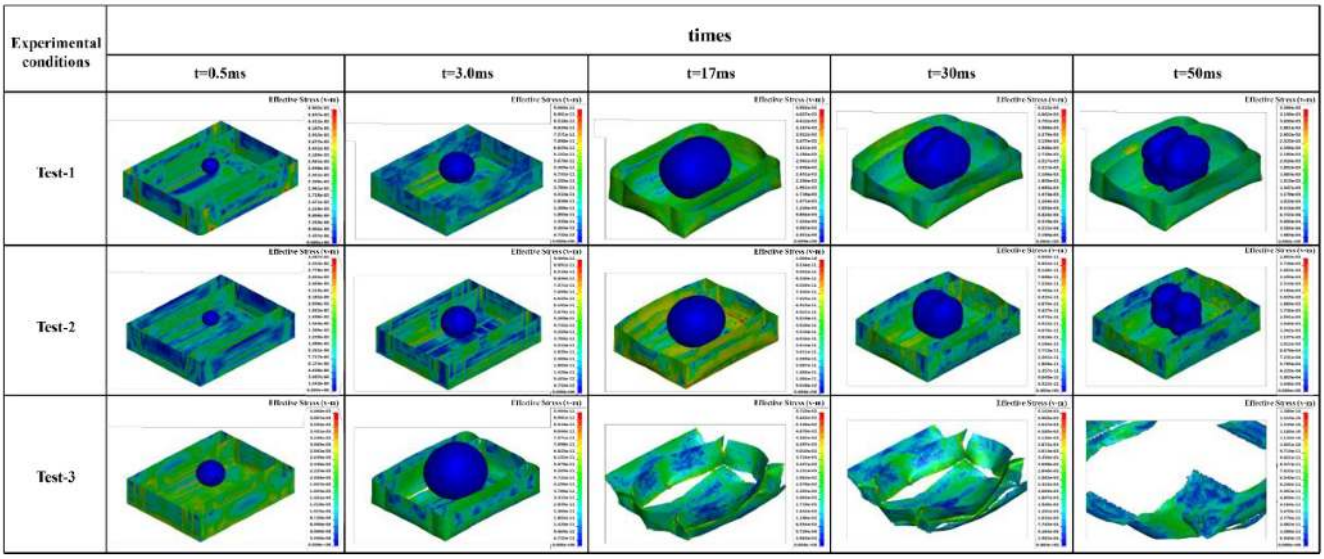


Figure 27: Strain contours of the three-compartment steel box under Test-1, Test-2, and Test-3

To further evaluate the individual contributions of the shock wave and the bubble to the plastic deformation of the adjacent cabins, the central elements of the inner and outer plates of the steel box are selected for detailed analysis. The dynamic responses of these plates in the adjacent cabins under the three test conditions are examined, and the corresponding time-history curves of effective stress, strain, and displacement at the central elements are presented in Figure 28.

The temporal trends of the response curves under Test-1 and Test-2 are generally consistent. Stress peaks occur in the inner and outer plates at approximately 190 and 310 μs, respectively. The peak stress values for the inner plate are 111.72 and 70.39 MPa under the two conditions, whereas those for the outer plate are 50.51 and 19.87 MPa. At these corresponding times, displacement begins to increase gradually, while the effective plastic strain shows no noticeable variation.

Taking Test-1 as an example, the inner plate reaches a stress peak of 130.80 MPa at approximately 2500 μs, corresponding to a displacement of 1.52 cm. At this stage, the effective plastic strain starts to increase, reaching 2.06×10^{-4} at 5000 μs. The outer plate attains a stress peak of 177.01 MPa at approximately 12,000 μs, corresponding to a displacement of 4.25 cm, and the effective plastic strain subsequently increases, reaching 7.31×10^{-5} at 18,000 μs. During the primary shock-wave phase within 800 μs, although relatively high stress levels are observed in both plates, the effective plastic strain remains essentially unchanged. During the dominant bubble expansion phase after 1000 μs, the effective plastic strain increases rapidly.

Under the Test-3 condition, effective plastic strains of 9.59×10^{-5} and 1.11×10^{-5} appear in the inner and outer plates at 475 and 935 μs, respectively, with the occurrence of the stress peak in the inner plate coinciding with the abrupt increase

in strain. At 900 μs, bubble-induced loading initiates plastic deformation in the inner plate, whereas the outer plate develops plastic strain at a later stage, around 6000 μs. The overall response occurs earlier than in Test-1 and Test-2, while the magnitude of plastic deformation in the outer plate remains smaller than that in the inner plate. This difference is associated with the separation of the adjacent cabins from the central cabin, causing the outer plates to move outward together with the adjacent cabins as integrated bodies. In addition, the outer plates undergo tearing during the ejection process, eventually detaching from the adjacent cabins, which results in progressively larger displacements than the inner plates. Consequently, the plastic deformation of both the inner and outer plates in the adjacent cabins is primarily governed by bubble expansion effects.

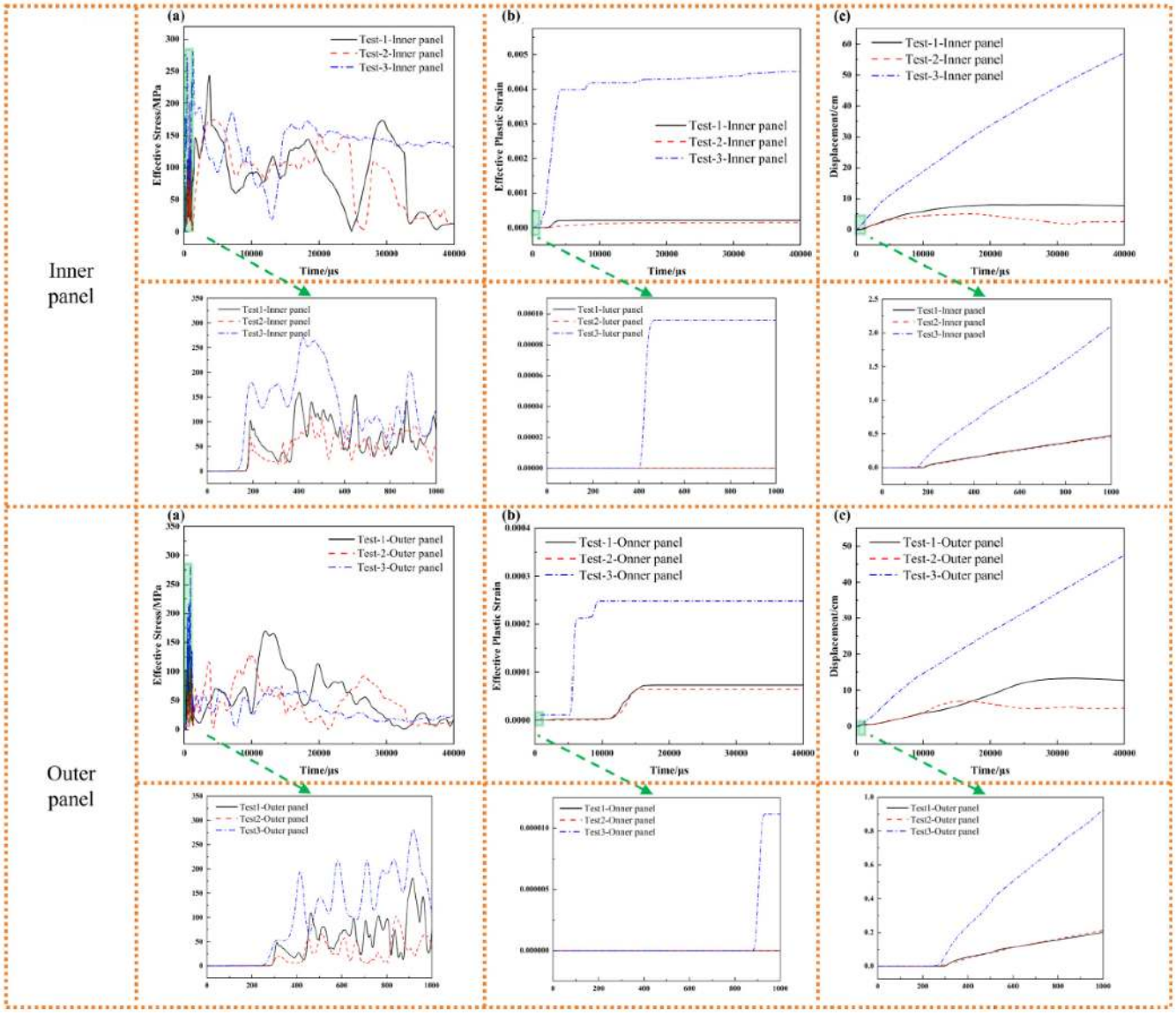


Figure 28: Response process of central elements of the inner and outer plates: (a) Effective stress; (b) Effective plastic strain; (c) Displacement

The final displacements of the inner plate under Test-1 and Test-2 are 7.78 and 2.62 cm, respectively, whereas those of the outer plate are 12.73 and 4.97 cm. The deformation magnitude of the outer plate exceeds that of the inner plate, which is attributed to the greater constraint imposed on the outward plastic deformation of the inner plate by the confined water medium within the adjacent cabin, in contrast to the relatively weaker constraint experienced by the outer plate under free-field conditions. Furthermore, the overall strain and deformation responses under Test-2 are smaller than those observed under Test-1, indicating that increasing wall thickness effectively reduces the deformation response.

5. Damage Characteristics of Adjacent Cabin Structures

Based on the above experimental and numerical results, the damage response of the submerged three-cabin structure under internal explosion loading is strongly influenced by parameters, such as charge mass and bulkhead thickness. To systematically examine the damage characteristics of adjacent cabins in a submerged three-cabin configuration subjected to internal blast loading under different charge masses and wall thicknesses, additional numerical simulations were carried out based on the experimental conditions, as summarized in Table 6. The constitutive models and corresponding material parameters adopted in the simulations are those previously validated and calibrated. To realistically represent a sealed underwater three-cabin structure, no pressure-relief openings were included in the top plates during model construction. In addition, to achieve a balance between computational accuracy and efficiency, a quarter-symmetry numerical model was employed for the simulations. (Table 7)

Table 6. Peak pressure of measurement points

Test ID	Distance/cm	Central Cabin (B10-11)	Adjacent Cabin (B4-5)	Attenuation Coefficient (α)
		Peak Value I/MPa	Peak Value I/MPa	
Test-1	40	30.53	26.60	0.87
	50	22.66	20.71	0.91
Test-2	40	29.99	20.73	0.69
	50	22.50	15.25	0.68
Test-3	40	105.91	74.47	0.75
	50	79.10	61.77	0.78

Table 7. Extended numerical simulation cases

Extended Case ID	Thickness/mm	Mass/g
EC1	1	50、100、150、
EC2	3	200、250、300

The damage morphologies of the submerged three-cabin structure with wall thicknesses of 1 and 3 mm under different charge masses are presented in Figures 29 and 30, respectively. Considering the 1-mm-thick case, at a relatively low charge mass of 50 g, the structure mainly exhibits plastic deformation, characterized by outward bulging of the panels and the formation of plastic hinge lines. When the charge mass increases to 100 g, rupture first occurs at the edge regions connecting the central cabin top plate and the side bulkheads, while the arching deformation of the top plate becomes more pronounced. The damage pattern is dominated by edge cracking initiating at the corners and propagating along the sides. At 150 g, complete tearing develops at the edge regions, and the fracture propagates along the side plates, forming a localized opening with a length of 45.34 cm. At 200 g, the cracks at the connections between the central cabin top plate and surrounding bulkheads become fully interconnected, and the structure enters a localized disintegration stage. The central cabin top plate detaches and is ejected, showing shear failure characterized by rapid separation around its perimeter. At 250 g, the integrity of the adjacent cabins is also compromised, and a 60.23 cm opening develops at the connection between the front outer plate and the cabin wall, originating from stress concentration at the edges induced by load transfer and sustained loading. At 300 g, complete disintegration of the central cabin occurs. However, the rapid release of bubble energy and flow field effects through the breach reduces the sustained loading acting on the adjacent cabins, resulting in a lower damage level than that under the 250-g condition. These results indicate that, for a fixed wall thickness, the damage mode of the adjacent cabins evolves with increasing charge mass from plastic deformation to edge cracking and ultimately to shear failure.

Under identical explosion loading conditions, the 1-mm-thick steel box undergoes severe disintegration within the charge mass range of 100–250 g. In this case, the central cabin top plate first tears along the connecting edges with the adjacent cabins, followed by progressive detachment and ejection, which ultimately leads to failure and fragmentation of the outer plates. The 3-mm-thick steel box exhibits a significantly higher damage threshold. In this configuration, the top plate initially tears at the edges adjacent to the neighboring cabins and subsequently develops cracks at the connections with the side plates. Global disintegration and panel ejection occur only under extremely high charge masses. These results indicate that an increase in wall thickness enhances the overall structural stiffness and energy

absorption capacity, raises the transition threshold of failure modes in the central cabin, and provides improved protective effectiveness for the adjacent compartments.

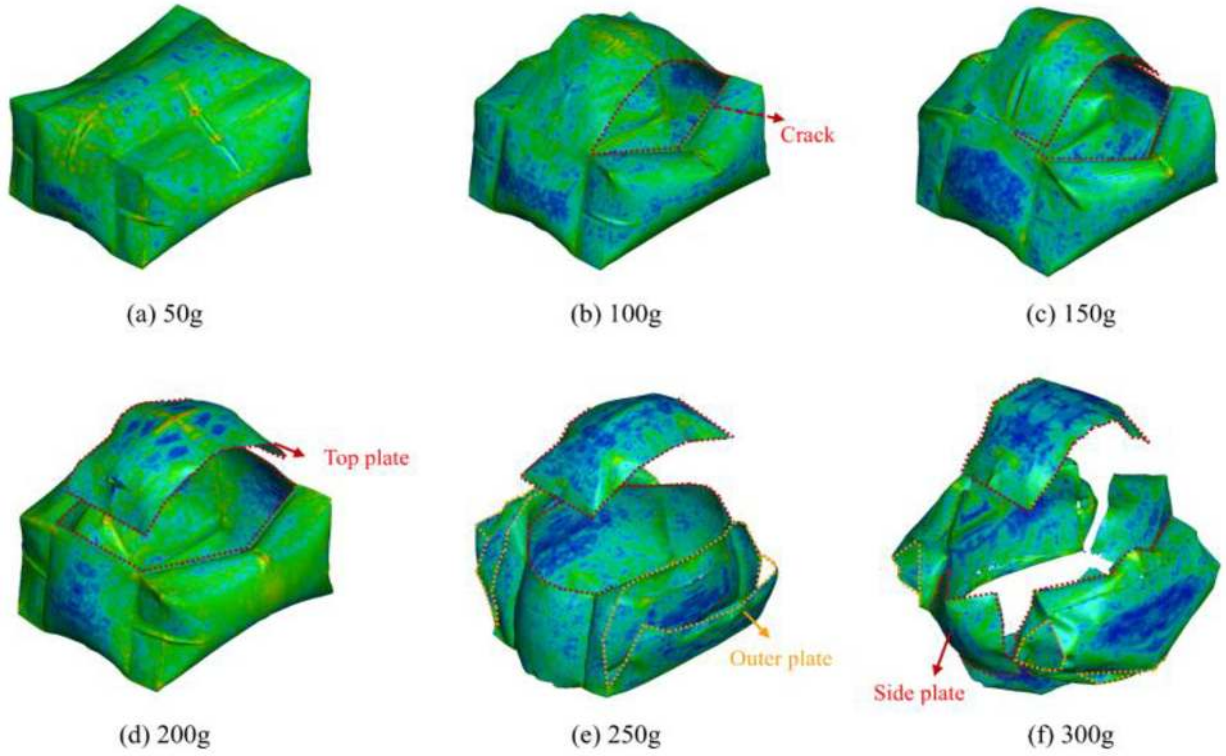


Figure 29: Damage strain contours of the underwater three-compartment structure with different charge masses under EC1

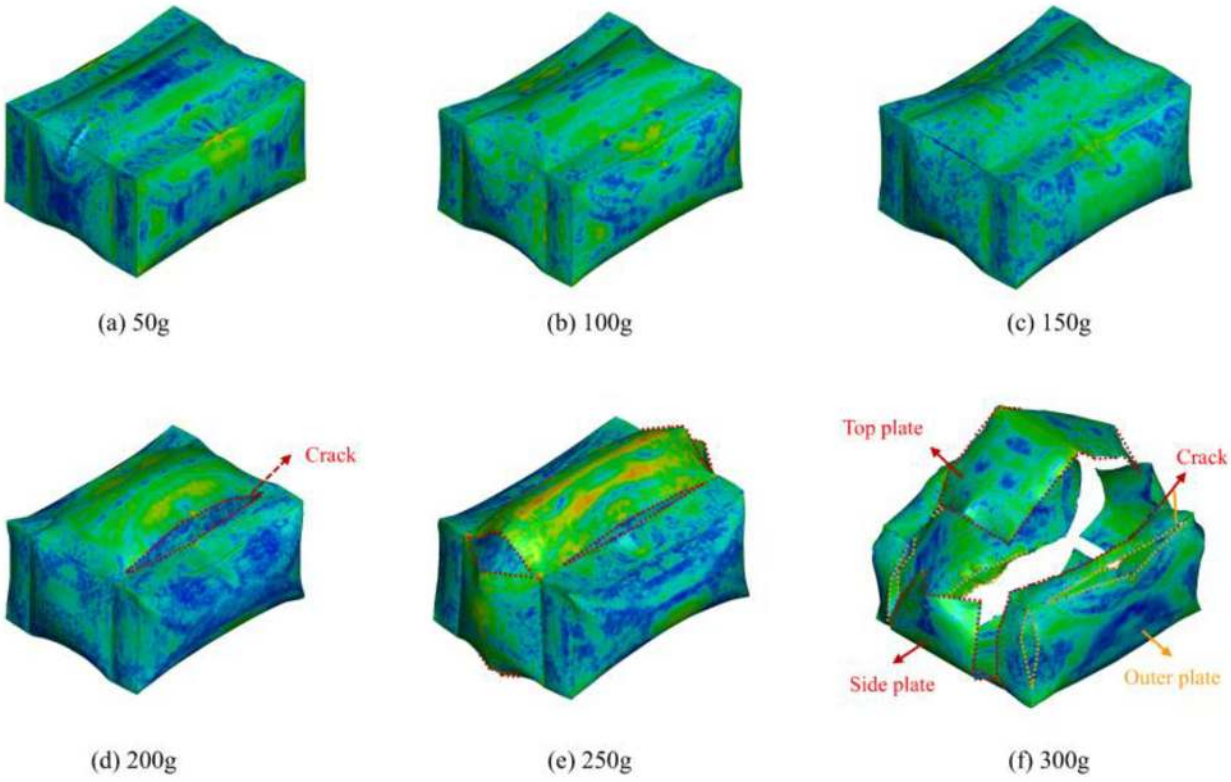


Figure 30: Damage strain contours of the underwater three-compartment structure with different charge masses under EC2

Based on a comparative analysis of the dynamic response and damage behavior of adjacent cabins under internal blast loading in the submerged box structure, the governing mechanisms responsible for the observed differences in damage morphology are clearly distinct.

Under relatively low charge mass conditions, the overall structure primarily undergoes global plastic deformation. During the shock-wave stage, the internally generated shock wave has a limited influence on the bulkhead plates within the box. In the subsequent bubble pulsation stage, the expanding bubble compresses the surrounding water medium inside the cabin, resulting in continuous pressure transmission to the top plate and inner plates of the central cabin. This induces outward deformation and expansion of both the top plate and inner plates away from the detonation center. At the same time, pressure is transferred through the inner plates via the water medium in the adjacent cabins, reaching the outer plates and leading to the development of plastic hinge lines. As the bubble subsequently contracts inward, the pressure within the adjacent cabins decreases, and localized rebound deformation occurs at the central regions of the outer plates. In addition, the thickness of the outer plate significantly affects the intensity of fluid motion within the adjacent cabin. For thicker bulkhead plates, the influence of fluid-induced motion is comparatively reduced, resulting in a corresponding decrease in the overall deformation of the plates.

Under relatively high charge mass conditions, the structure exhibits edge-tearing failure. The bubble expands rapidly to a large volume, producing strong compression on the walls of the central cabin. The top plate, which is subjected to relatively lower water resistance from above, undergoes upward bulging deformation first. As plastic deformation develops in the inner and side plates, relative rotation and tensile effects are preferentially concentrated at the mid-region of the weld seam between the top plate and the inner plates. Fracture occurs once the combined tensile and rotational loading exceeds the weld strength. Continued bubble expansion further propagates and extends the existing cracks, while bubble venting through the fractured regions promotes additional crack growth and intensifies the arching deformation of the top plate. A similar failure mechanism occurs at other connections: when the combined tensile and rotational effects induced by the plastic deformation of the outer plates and the top plate exceed the weld strength, fracture also develops along the corresponding edges. Since bubble penetration into the adjacent cabins is limited, the deformation of the adjacent cabin top plates is generally smaller than that of the central cabin top plate, and the severity of edge failure in the adjacent cabins is lower than that observed at the weld interface between the central cabin top plate and the inner plates.

Under extremely large charge mass conditions, the central cabin undergoes shear failure, leading to the separation of individual bulkhead plates, while the front and rear cabins exhibit rigid-body translation. This behavior is attributed to the fact that the shear strength of the weld seams between plates is significantly lower than that of the base material. Under the rapidly increasing pressure generated by the expanding bubble, the high load induces shear failure along the plate connections. In this case, the inner plates do not experience pronounced plastic deformation, and the pressure transmitted to the water medium within the adjacent cabins due to inner plate deformation is correspondingly limited. As a result, the adjacent cabins remain largely intact and translate as integral structural units.

Overall, the damage pattern and severity of the adjacent cabin evolve progressively with increasing charge mass in the central cabin. For the 1-mm-thick steel box, global plastic deformation occurs at 50 g; corner rupture of the central cabin top plate and severe plastic deformation of the adjacent cabin appear at 100 g; a 60.23 cm breach forms at the corner of the adjacent cabin outer plate at 250 g; and disintegration of the central cabin accompanied by integral ejection of the adjacent cabin takes place at 300 g. These damage modes correspond to distinct governing mechanisms: global plastic deformation is dominated by bubble pulsation pressure transmitted via the water medium; corner tearing is triggered when the combined tension-rotation loading on the top plate–inner plate welds, induced by rapid bubble expansion, exceeds the material strength; and disintegration and integral ejection of the adjacent cabin are governed by shear fracture of the weld seams. In addition, increased wall thickness significantly mitigates adjacent cabin damage: the 1-mm-thick box suffers severe disintegration at 100 g, while the 3-mm-thick box only develops cracks at 200 g.

6. Conclusion

In this study, experimental and numerical simulation approaches were employed to investigate the dynamic response and damage characteristics of adjacent cabins subjected to internal explosion loading in a submerged thin-walled box structure. The main conclusions are as follows:

1. After internal explosion in a submerged thin-walled central cabin, water pressure in both cabins exhibits multiple peaks and a prolonged positive duration. Peaks in the central cabin originate from direct shock waves and repeated boundary reflections, while those in adjacent cabins result from partition-transmitted shocks,

multi-reflection superposition and bubble pulsation. The attenuation coefficient drops from 0.89 (1-mm steel) to 0.73 (3-mm steel) with increasing partition thickness.

2. Bubble expansion and contraction mainly occur in the charged central cabin or escape through structural ruptures, the volume and evolution in adjacent cabins are governed by inner plate perforations. Bubbles cannot enter adjacent cabins through intact inner plates; once they invade adjacent cabins via perforations, reverse intrusion of pressurized cabin water into the bubble interior triggers bubble collapse.
3. Deformation and rupture of adjacent cabin walls are dominated by bubble expansion, with pressure loads transmitted via the incompressible water medium. Two mechanisms account for the pressure rise in adjacent cabins: outward bulging of the inner plate driven by central cabin bubbles compresses the cabin volume and transfers pressure to the outer plate; direct invasion of bubbles through inner plate perforations further elevates the internal pressure.
4. The damage pattern and severity of adjacent cabins evolve progressively with increasing charge mass. Under small charges, bubble expansion bulges the inner plate via water mediation, raising cabin pressure and inducing outer plate plastic deformation. Under moderate charges, rapid bubble expansion causes severe plastic deformation, with cracks initiating at structural corners and propagating into corner tearing under bubble extrusion. Under larger charges, shear failure occurs in the central cabin, and the adjacent cabin is ejected integrally with mild outer plate deformation. Increased wall thickness significantly mitigates damage: the 1-mm box suffers completely disintegrated at 100 g, while the 3-mm box only develops cracks at 200 g.

Author's Contribuitions: Writing-original draft, Yiming Ma; Test technical support, Xingbo Xie, Guili Yang; Writing-review & editing, Huayuan Ma; Numerical simulation technical support, Xinghua Li, Mingshou Zhong.

Data availability statement: Research data is only available upon request.

Editor: Marcilio Alves.

References

Babu V, Kulkarni K, Kankanalapalli S, et al. Comparative analysis of occupant responses between LS-DYNA® arbitrary LaGrange in Euler and (ALE) and structured–ALE (S-ALE) methods[C]//15th International LS-DYNA Conference. 2018.

Cheng L, Huang F, Wu H, et al. Comparative analysis of blast load transfer and structural damage in multi-cabin structures during air and underwater explosions[J]. Ocean Engineering, 2024a, 297: 116953.

Cheng L, Huang F, Wu H, et al. Cumulative damage effects of repeated underwater explosions on multi-cabin structures[J]. Thin-Walled Structures, 2024b, 204: 112231.

Fei H, Xie X, Yang G, et al. Experimental and numerical investigation of the damage effects in an underwater confined box subjected to internal blast loading[J]. Journal of Applied Physics, 2025, 137(14).

Gao H, Wang Y, Zhai X. Numerical and analytical studies of multi-cell steel-concrete-steel sandwich panels under blast load[C]//Structures. Elsevier, 2024, 63: 106452.

He Z, Du Z, Zhang L, et al. Damage mechanisms of full-scale ship under near-field underwater explosion[J]. Thin-Walled Structures, 2023, 189: 110872.

Jin, Hou H, Chen P, et al. Experimental study on the combined damage of liquid cabin structure subjected to charge explosion with preset fragments[J]. International Journal of Impact Engineering, 2019, 130: 19-26.

Kristoffersen M, Minoretti A, Børvik T. On the internal blast loading of submerged floating tunnels in concrete with circular and rectangular cross-sections[J]. Engineering failure analysis, 2019, 103: 462-480.

Lee S G, Lee H S, Lee J S, et al. Shock response analysis of blast hardened bulkhead in partial chamber model under internal blast[J]. Procedia Engineering, 2017, 173: 511-518.

Li Y, Zhang L, Xiao D, et al. Experiment and numerical study on dynamic response of liquid cabin under internal blast loading[J]. Thin-Walled Structures, 2019, 145: 106405.

Lin X, Wang S, Zhang L, et al. Study on load characteristics and structural impact response propagation law of cabin internal explosion[J]. Ocean Engineering, 2024, 301: 117582.

Peng Y X, Zhang A M, Ming F R. Numerical simulation of structural damage subjected to the near-field underwater explosion based on SPH and RKPM[J]. Ocean Engineering, 2021, 222: 108576.

Pickerd V, Bornstein H, McCarthy P, et al. Analysis of the structural response and failure of containers subjected to internal blast loading[J]. International Journal of Impact Engineering, 2016, 95: 40-53.

Qin Y, Yao X, Wang Z, et al. Experimental investigation on damage features of stiffened cabin structures subjected to internal blast loading[J]. Ocean Engineering, 2022, 265: 112639.

Tørnes J A, Novik G P. Evaluating the environmental impact of leaking WW2 shipwrecks: A closer look at the VRAKA and AmuCad decision support tools[J]. Marine Pollution Bulletin, 2025, 215: 117930.

Wang G, Wang Y, Lu W, et al. On the determination of the mesh size for numerical simulations of shock wave propagation in near field underwater explosion[J]. Applied Ocean Research, 2016, 59: 1-9.

Wang H, Pei D, Zhang P, et al. The plastic dynamics and failure analysis of ship broadside protection structures subjected to contacted UNDEX: energy dissipation model and simulation[J]. Ships and Offshore Structures, 2022, 17(4): 728-741.

Wang Y, Li W, Zhu W, et al. Dynamic response of steel cabin structure under blast loading from adjacent cabin[J]. Engineering Structures, 2024, 311: 118213.

Wang Z, Gao Y, Zhang Y, et al. Analysis of damage characteristics of the rectangular steel container under near-earth explosion loading[J]. Case Studies in Construction Materials, 2024, 21: e03518.

Yao S, Chen F, Wang Y, et al. Experimental and numerical investigation on the dynamic response and damage of large-scale multi-box structure under internal blast loading[J]. Thin-Walled Structures, 2023, 183: 110430.

Yao S, Zhang D, Lu F, et al. Experimental and numerical studies on the failure modes of steel cabin structure subjected to internal blast loading[J]. International Journal of Impact Engineering, 2017, 110: 279-287.

Yuan Y, Zhang C, Xu Y. Influence of standoff distance on the deformation of square steel plates subjected to internal blast loadings[J]. Thin-Walled Structures, 2021, 164: 107914.

Zhang C, Tan P J, Yuan Y. Confined blast loading of steel plates with and without pre-formed holes[J]. International Journal of Impact Engineering, 2022, 163: 104183.

Zhang X, He Z, Du Z, et al. Multi-peak phenomenon of large-scale hull structural damage under near-field underwater explosion[J]. Ocean Engineering, 2023, 283: 114898.

Zhao N, Yao S, Zhang D, et al. Experimental and numerical studies on the dynamic response of stiffened plates under confined blast loads[J]. Thin-Walled Structures, 2020, 154: 106839.

Zheng C, Kong X, Wu W, et al. The elastic-plastic dynamic response of stiffened plates under confined blast load[J]. International Journal of Impact Engineering, 2016, 95: 141-153.

Zheng C, Kong X, Wu W, et al. Experimental and numerical studies on the dynamic response of steel plates subjected to confined blast loading[J]. International Journal of Impact Engineering, 2018, 113: 144-160.